

# PREDICTING THE EXTREME ULTRAVIOLET RADIATION ENVIRONMENT OF EXOPLANETS AROUND LOW-MASS STARS: GJ 832, GJ 176, GJ 436

SARAH PEACOCK,<sup>1</sup> TRAVIS BARMAN,<sup>1</sup> EVGENYA L. SHKOLNIK,<sup>2</sup> PETER H. HAUSCHILDT,<sup>3</sup> E. BARON,<sup>4,3</sup> AND BIRGIT FUHRMEISTER<sup>3</sup>

<sup>1</sup>*University of Arizona, Lunar and Planetary Laboratory, 1629 E University Boulevard, Tucson, AZ 85721, USA*

<sup>2</sup>*School of Earth and Space Exploration, Arizona State University, Tempe, AZ 85281, USA*

<sup>3</sup>*Hamburger Sternwarte, Gojenbergsweg 112, D-21029 Hamburg, Germany*

<sup>4</sup>*Homer L. Dodge Department of Physics and Astronomy, University of Oklahoma, 440 W. Brooks, Rm 100, Norman, OK 73019-2061 USA*

(Accepted October 17, 2019)

Submitted to ApJ

## ABSTRACT

Correct estimates of stellar extreme ultraviolet (EUV; 100 – 1170 Å) flux are important for studying the photochemistry and stability of exoplanet atmospheres, as EUV radiation ionizes hydrogen and contributes to the heating, expansion, and potential escape of a planet’s upper atmosphere. Contamination from interstellar hydrogen makes observing EUV emission from M stars particularly difficult, and impossible past 100 pc, and necessitates other means to predict the flux in this wavelength regime. We present EUV – infrared (100 Å – 5.5 μm) synthetic spectra computed with the PHOENIX atmospheric code of three early M dwarf planet hosts: GJ 832 (M1.5 V), GJ 176 (M2.5 V), and GJ 436 (M3.5 V). These one-dimensional semiempirical nonlocal thermodynamic equilibrium models include simple temperature prescriptions for the stellar chromosphere and transition region, from where ultraviolet (UV; 100 – 3008 Å) fluxes originate. We guide our models with *Hubble Space Telescope* far- and near-UV spectra and discuss the ability to constrain these models using *Galaxy Evolution Explorer* UV photometry. Our models closely reproduce the observations and predict the unobservable EUV spectrum at a wavelength resolution of <0.1 Å. The temperature profiles that best reproduce the observations for all three stars are described by nearly the same set of parameters, suggesting that early M type stars may have similar thermal structures in their upper atmospheres. With an impending UV observation gap and the scarcity of observed EUV spectra for stars less luminous and more distant than the Sun, upper-atmosphere models such as these are important for providing realistic spectra across short wavelengths and for advancing our understanding of the effects of radiation on planets orbiting M stars.

*Keywords:* stars: activity, stars: chromospheres, stars: low-mass, ultraviolet: stars

## 1. INTRODUCTION

The majority of known terrestrial-sized exoplanets located within the canonical habitable zone are found orbiting M stars (Shields et al. 2016), including the most nearby, Proxima Centauri b (Anglada-Escudé et al. 2016) and three of the seven TRAPPIST-1 system planets (Gillon et al. 2017). Due to their cool effective temperatures ( $\sim 3,000$  K), the canonical habitable zone around M stars is close in, extending from 0.1 to 0.4 au. Their low masses and luminosities allow for easier detection of small, transiting rocky planets orbiting at small separations, occurring at a rate of 0.1 to 0.6 planets per star (Dressing & Charbonneau 2013; Kopparapu 2013; Dressing & Charbonneau 2015). An increasing number of exoplanet detections around low-mass stars, particularly those located at short periods, motivates the need to understand the properties of low-mass parent stars.

The stellar ultraviolet (UV, 100 – 3008 Å) environment around M stars strongly impacts the formation, evolution, and chemistry of close-in exoplanet atmospheres. Due to phenomena occurring in the outer layers of these stars, most M stars have significant long-term UV variability leading to large amounts of short wavelength emission during their active periods (Shkolnik & Barman 2014; Loyd et al. 2018a,b; Schneider & Shkolnik 2018). The increased levels of UV radiation can alter the chemical composition of planetary atmospheres and lead to significant mass loss, with different wavelengths in a stellar spectrum driving heating and chemistry in different layers of a planet’s atmosphere.

Stellar far-UV (FUV; 1150 – 1700 Å) radiation photodissociates molecules including  $\text{CO}_2$ ,  $\text{CH}_4$ , and  $\text{H}_2\text{O}$  in the upper atmospheres of planets (Segura et al. 2005; Hu et al. 2012; Moses 2014; Rugheimer et al. 2015; Loyd et al. 2016). For example, the strongest emitting line in the FUV, Lyman  $\alpha$  ( $\text{Ly}\alpha$ ; 1215.7 Å), will generate hydrocarbon hazes in the upper atmospheric layers as a direct result of dissociating methane in a planet’s ionosphere (Trainer et al. 2006). At longer wavelengths, stellar near-UV (NUV; 1680 – 3008 Å) flux dissociates both  $\text{O}_2$  and  $\text{O}_3$ . Analyzing single and repeated UV flare events and from the M dwarf star, AD Leo, Segura et al. (2010) and Tilley et al. (2019) found that the combination of UV radiation and protons is capable of depleting almost all of the  $\text{O}_3$  on an Earth-like planet in an M star’s habitable zone in under 10 years.

Close-in exoplanets become vulnerable to mass loss as stellar extreme-UV (EUV; 100 – 1170 Å) radiation ionizes hydrogen. This process heats and expands the atmospheric layers above the planet’s thermosphere, potentially leading to ion pickup by the stellar wind or hydrodynamic outflow of hydrogen (Lammer et al. 2007;

Tian et al. 2008; Murray-Clay et al. 2009; Koskinen et al. 2010; Rahmati et al. 2014; Chadney et al. 2015; Tripathi et al. 2015). Depending on the amount of EUV flux they are exposed to, habitable zone planets around M stars can lose both oceans and significant fractions of their atmospheres within a few billion years (Luger & Barnes 2015). Correct estimates of stellar EUV flux are important for studying the stability of exoplanet atmospheres and the stability of the M star habitable zone.

Observing in EUV wavelengths is extremely difficult due to optically thick interstellar hydrogen absorbing most of the spectrum between 400 – 912 Å (Barstow & Holberg 2007). While the quantity of absorption due to the interstellar medium (ISM) is dependent on the direction, short-wavelength UV observations are significantly affected for nearly all planet-hosting stars ( $>100$  pc) making them possible only for systems closer than 50 – 100 pc (Fossati et al. 2017). Over the course of the mission, the *Extreme Ultraviolet Explorer* (*EUVE*) observed six active M stars with low signal-to-noise from 100 – 400 Å (AD Leo, AU Mic, EV Lac, Proxima Centauri, YY Gem, YZ CMI). The majority of the EUV emission from these stars is below the minimum detectable flux level for the instrument, so only strong emission lines including He II and highly ionized iron (Fe IX – XVI) were identified (Craig et al. 1997). No flux was observed from 350-912 Å. While current capabilities allow for FUV, NUV, and limited X-ray measurements, there are no operational instruments able to observe stars other than the Sun in the EUV wavelength range.

Due to the scarcity of EUV observations for M stars, studies have relied on using either the *EUVE* spectrum of the very active M star, AD Leo (Segura et al. 2010; Wordsworth et al. 2010), or other proxies to determine the flux in this wavelength regime. Current methods to predict EUV flux include various empirical scaling relationships (Linsky et al. 2014; Chadney et al. 2015; France et al. 2018) and semiempirical models to produce synthetic EUV spectra (e.g. Lecavelier Des Etangs 2007; Sanz-Forcada et al. 2011; Fontenla et al. 2016; Peacock et al. 2019). Stellar EUV spectra are characterized by many emission lines with large dynamic ranges in flux, superimposed on a continuum marked with distinct bound-free edges from continuous opacity sources. In a low activity solar spectrum, the strongest EUV emission lines peak at fluxes three orders of magnitude larger than continuum levels (Tobiska 1996). This level of detail is not encompassed in broadband scaling relationships and can only be predicted with high resolution synthetic spectra. The radiation in individual EUV emission lines penetrates planetary atmospheres at

different depths, affecting the ionization rates and likelihood for escape. It is therefore important to include high resolution stellar EUV spectra rather than single valued fluxes when modeling both the photochemistry and escape in exoplanet atmospheres.

There has been significant effort to produce semiempirical models for the Sun (e.g. Vernazza et al. 1981; Fontenla et al. 1990) that utilize the wealth of solar observations across all wavelengths to validate the temperature structure. The flux in different wavelength regions emerges from different depths in a stellar atmosphere, providing important constraints on the thermal structure. Early modeling of M type stars used ground-based observations of chromospheric lines found in optical wavelengths to determine the temperature structure in the chromosphere (e.g. Giampapa et al. 1982; Andretta et al. 1997; Short & Doyle 1998; Fuhrmeister et al. 2005)<sup>1</sup>. In order to determine the temperature structure in the full upper atmosphere and estimate realistic EUV spectra, X-ray and/or UV observations are needed to guide and validate semiempirical stellar models. It is important to note that the timescales for flares and magnetic activity cycles occurring in the upper-atmospheric layers of M stars ranges from seconds to years and results in highly variable levels of measured X-ray and UV flux (Monsignori Fossi et al. 1996; Hawley et al. 2003; Stelzer et al. 2013; Loyd et al. 2018a,b). As a result, models based on non-contemporaneous X-ray and UV observations will have potentially large uncertainties in the predicted EUV spectra.

Stellar X-ray measurements provide important information about the thermal structure in the outermost  $\sim 10^6$  K coronal layers, where emission features of highly ionized species found in the XUV (1 – 912 Å) spectrum form. The EUV continuum and many FUV emission lines, however, form at cooler temperatures deeper in the stellar atmosphere in the chromosphere and transition region. Estimating UV spectra using only X-ray observations leads to systematically underpredicted line fluxes because the X-ray observations do not include the contribution from the deeper atmospheric layers. For example, Sanz-Forcada et al. (2011) used emission measure distribution coronal models with *XMM-Newton*, *Chandra*, and *ROSAT* X-ray observations to compute synthetic XUV spectra of 82 late-F to mid-M planet hosts, but the spectra were found to underpredict observed FUV line strengths by up to a factor of 33 (France et al. 2016; Loudén et al. 2017).

The majority of spectral features observed in the stellar UV spectrum form at temperatures ranging from  $10^4$  –  $10^6$  K (Sim & Jordan 2005). While FUV and NUV observations lack major contribution from the corona (with notable exception of the Fe XII line at 1242 Å that forms near  $1.4 \times 10^6$  K), they provide crucial information about the thermal structure in the chromosphere and transition region, where a large fraction of EUV emission is generated. Recently, Peacock et al. (2019) used the PHOENIX atmosphere code to predict the EUV through near-IR spectrum of the M8 star TRAPPIST-1, calibrating the models with two UV datasets. The models have temperature-pressure profiles qualitatively similar to the Sun, but without a corona. The models reproduce the UV observations well and predict EUV fluxes consistent with estimates calculated using empirical scaling relationships. However, as a result of not including the coronal flux contribution, they are estimated to underpredict the spectrum at wavelengths  $< 300$  Å. Fontenla et al. (2016) adapted their solar model (Fontenla et al. 2007, 2009, 2011, 2014, 2015) to produce a full upper atmosphere model for the M1 star GJ 832 that covers X-ray through optical wavelengths and provides the first spectrally resolved EUV prediction for this star.

In this paper, we present 1D nonlocal thermodynamic equilibrium (non-LTE) synthetic spectra (EUV – IR, 100 Å – 5.5  $\mu$ m) of three early-M planet host stars (GJ 832, GJ 176, GJ 436) that replicate both *Hubble Space Telescope* (*HST*) and *Galaxy Evolution Explorer* (*GALEX*) observations of each target. We show that constructing models with a simple temperature structure can reproduce the UV continuum and many emission features in high resolution *HST* spectra. These models also predict the unobservable EUV spectrum, as they include prescriptions for the stellar upper atmosphere, including the chromosphere and transition region, where EUV, FUV, and NUV fluxes originate.

In Section 2, we describe the construction and specifications in our atmospheric models. In Section 3, we discuss the properties and pre-existing observations of our target stars that we use to guide our models. We analyze the computed spectra and compare them to optical and UV observations in Section 4. The synthetic EUV spectra are described in Section 5. In Section 6, we compare our models to flux estimates derived from empirical scaling relationships and semiempirical modeling. Conclusions are given in Section 7.

## 2. MODEL

We build 1D stellar upper atmosphere models with prescriptions for the chromosphere and transition re-

<sup>1</sup> For a complete summary of previous semiempirical chromosphere models for Main Sequence stars, see Linsky (2017).

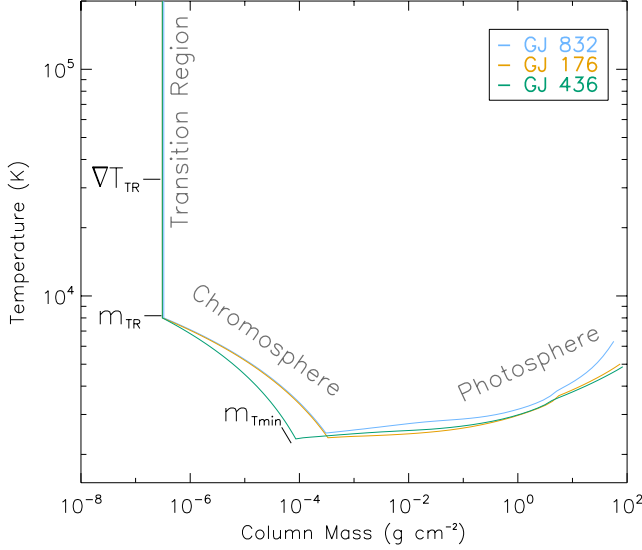


**Figure 1.** Temperature-column mass structures for models of GJ 832 (blue), GJ 176 (orange), and GJ 436 (green) with prescriptions for the chromosphere and transition region. The radiative-convective boundary in the photosphere for all three models occurs around  $8 \text{ g cm}^{-2}$ . Free parameters in the construction of the upper atmosphere are the column mass at the base and top of the chromosphere:  $m_{Tmin}$  and  $m_{TR}$ , and the temperature gradient in the transition region:  $\nabla T_{TR}$  (approximate locations labeled). The parameter values for these models are given in Table 1.

gion using the multi-level non-LTE code PHOENIX (Hauschildt 1993; Hauschildt & Baron 2006; Baron & Hauschildt 2007). PHOENIX has been used to study the diagnostic properties of strong chromospheric lines in the optical spectrum of M stars (Hauschildt et al. 1996; Andretta et al. 1997; Short & Doyle 1998; Fuhrmeister et al. 2005, 2006; Hintz et al. 2019) and to create EUV – IR spectra of the M8 star, TRAPPIST-1 (Peacock et al. 2019).

For our models, we use a similar prescription to that used in Peacock et al. (2019). We begin with a base photosphere model in radiative-convective equilibrium that corresponds to the effective temperature, surface gravity, and mass of each star. We then superimpose an increasing temperature distribution up to 8,000 K to simulate a chromosphere and a steep temperature gradient above 8,000 K to simulate the transition region (Figure 1). At temperatures greater than  $\sim 8,000 \text{ K}$ , neutral hydrogen, the major source of electrons, is severely depleted by ionization and is no longer an efficient cooling agent. If heating decreases outward more slowly than column mass, then the chromosphere becomes thermally unstable, leading to the onset of the transition region. Stability is reattained near coronal temperatures where heat conduction and stellar wind losses dominate the

**Table 1.** Model Parameters

Model	$\nabla T_{TR}$ (K $\text{dyne}^{-1} \text{cm}^2$ )	$m_{TR}$ (g $\text{cm}^{-2}$ )	$m_{Tmin}$ (g $\text{cm}^{-2}$ )	$P_{out}$ (dyne $\text{cm}^{-2}$ )
GJ 832	$10^9$	$10^{-6.5}$	$10^{-3.5}$	0.016
GJ 176	$10^9$	$10^{-6.5}$	$10^{-3.5}$	0.02
GJ 436	$10^9$	$10^{-6.5}$	$10^{-4}$	0.02

plasma energy balance (Ayres 1979). In our models, we set the hottest layer at the top of the transition region to be 200,000 K, since the majority of observed emission lines in M star UV spectra form at or below this temperature, e.g. Mg II ( $\sim 10^{4.2} \text{ K}$ ), C II ( $10^{4.3} \text{ K}$ ), H I ( $\sim 10^{4.5} \text{ K}$ ), Si IV ( $10^{4.78} \text{ K}$ ), He II ( $\sim 10^{4.9} \text{ K}$ ), C IV ( $10^{4.98} \text{ K}$ ), N V ( $10^{5.22} \text{ K}$ ) (Sim & Jordan 2005).

Heating mechanisms in M dwarf chromospheres are not well understood. Acoustic heating, magnetic heating, and back irradiation from coronal layers are all suggested potential contributing processes (Narain & Ulmschneider 1996). For our models, we assume a linear temperature rise with  $\log(\text{column mass})$  in both the chromosphere and transition region. Previous works have experimented with implementing nonlinear  $\log(\text{column mass})$ -temperature profiles and found that nonlinear temperature rises can be tailored to replicate individual lines very well, but linear rises give the best overall continuum fit (Eriksson et al. 1983; Andretta et al. 1997; Fuhrmeister et al. 2005). For example, Fuhrmeister et al. (2005) altered the structure of the lower chromosphere in order to better fit observations of Na I D lines, but found that it resulted in worse fit models with significantly increased flux in the Balmer lines.

In the construction of the upper atmosphere, we alter three free parameters designating the depth at which the upper atmosphere is attached to the underlying photosphere and the thickness of both the chromosphere and transition region (approximate locations labeled in Figure 1). The specific parameters are the column mass at the initial chromospheric temperature rise ( $m_{Tmin}$ ), the column mass at the top of the chromosphere ( $m_{TR}$ ), and the temperature gradient in the transition region ( $\nabla T_{TR} = |dT/d \log P|$ ). We then use the prescriptions selected for each model to calculate the outer pressure:

$$P_{out} = \frac{T_{max} - T_{ch}}{\nabla T_{TR}} + (m_{TR} * g) \quad (1)$$

where  $T_{max}$  is the temperature at the top of the transition region, set to 200,000 K,  $T_{ch}$  is the temperature at the base of the transition region, set to 8,000 K, and  $g$  is

**Table 2.** Species computed in non-LTE

Element	Abundance	Levels						Total Lines
		I	II	III	IV	V	VI	
H	12.0	30	...	...	...	...	...	435
He	10.93	19	10	...	...	...	...	82
C	8.43	230	85	79	36	...	...	4,216
N	7.83	254	152	87	81	...	...	5,537
O	8.69	146	171	137	138	...	...	3,466
Ne	7.93	26	279	...	...	...	...	3,516
Na	6.24	58	35	69	...	...	...	858
Mg	7.6	179	74	90	54	...	...	2,972
Al	6.45	115	191	58	...	...	...	3,432
Si	7.51	330	93	163	52	...	...	6,001
P	5.41	230	90	...	...	...	...	1,827
S	7.12	152	84	41	...	...	...	2,666
Cl	5.5	278	124	78	...	...	...	8,314
Ar	6.4	208	302	96	...	...	...	7,652
K	5.08	80	22	38	...	...	...	834
Ca	6.34	196	89	150	...	...	...	4,730
Ti	4.95	555	204	185	39	...	...	18,317
V	3.93	483	323	299	...	...	...	17,246
Cr	5.64	392	733	214	...	...	...	23,464
Mn	5.43	297	512	391	...	...	...	17,214
Fe	7.5	902	894	555	276	180	93	62,791
Co	4.99	364	255	213	...	...	...	11,548
Ni	6.22	180	670	344	...	...	...	26,063

the surface gravity of the star. For each star, we create a grid of 29 models varying  $m_{Tmin} = 10^{-6} - 10^{-3.5}$  g cm $^{-2}$ ,  $m_{TR} = 10^{-7} - 10^{-6}$  g cm $^{-2}$ , and  $\nabla T_{TR} = 10^8 - 10^{10}$  K dyne $^{-1}$  cm $^2$ .

Different states of stellar activity are simulated by adjusting where the chromospheric temperature rise is attached to the underlying photosphere model (Andretta & Giampapa 1995; Andretta et al. 1997). Higher activity states, and therefore, higher UV continuum fluxes, are generated by shifting the temperature structure uniformly inward, beginning the initial temperature rise at larger column mass. Since many FUV emission features form at similar temperatures to those that are found in the EUV spectrum (Kretzschmar et al. 2009), both wavelength regimes are most sensitive to the same parameters:  $\nabla T_{TR}$  and  $m_{TR}$ . A factor of 10 decrease in  $\nabla T_{TR}$  or increase in  $m_{TR}$  results in an order of magnitude increase in the integrated flux density across EUV wavelengths and a factor of five increase in the integrated FUV flux density. Changes in  $m_{Tmin}$  correspond to changes in the strength of the extended wings of Ly $\alpha$

and therefore the FUV pseudo-continuum, but have a larger effect on the NUV spectrum. Adjusting the depth of the chromosphere by shifting the position where the temperature rise begins inwards by 10 g cm $^{-2}$  increases the NUV flux density by a factor of three and the FUV flux density by up to a factor of two. Changes in  $m_{Tmin}$  by itself have no effect on the computed EUV spectrum.

### 2.1. Microturbulent Velocity

Levels of microturbulent velocity ( $v_{turb}$ ) influence the intensity and wing shape of emission lines, particularly affecting hydrogen, sodium, and calcium lines (Jevremović et al. 2000). The turbulent surface of a stellar photosphere induces disturbances in the overlying chromosphere that are propagated at the speed of sound. For our models, we set  $v_{turb}$  to 2 km s $^{-1}$  in the photosphere and 10 km s $^{-1}$  at the top of the transition region. We follow the same approach as Fuhrmeister et al. (2005) in setting the slope of  $v_{turb}$  in the chromosphere and lower transition region to a fraction of the sound speed in each layer, but not allowing this value to ex-



ceed  $10 \text{ km s}^{-1}$ . We select a value of  $0.35 \times v_{\text{sound}}$  such that  $v_{\text{turb}}$  smoothly transitions from  $2 \text{ km s}^{-1}$  in the photosphere to the larger values in the chromosphere.

### 2.2. Non-Local Thermodynamic Equilibrium Radiative Transfer

In an M dwarf photosphere, temperatures are low and densities are high, such that collisions dominate and LTE is an appropriate approximation for calculating the level populations of atoms and molecules. As temperatures increase in the upper atmosphere and densities become very low, radiative rates exceed collisional rates and radiative transfer is dominated by non-LTE effects. PHOENIX is equipped with current atomic level data (Dere et al. 1997; Kurucz 2014, 2017; Del Zanna et al. 2015) suitable for these high temperatures and low densities and has the capacity to do multi-line non-LTE calculations for many species. For our models, we consider a total of 15,355 levels and 233,871 emission lines when computing the set of 73 atoms and ions listed in Table 2 in full non-LTE radiative transfer using species and background opacities provided by the PHOENIX and CHIANTI v8 databases (Landi et al. 2006). Also included in our models are new bound-free molecular opacities described in Peacock et al. (2019) and millions of optically thin atomic and molecular background lines calculated with assuming an LTE source function.

### 2.3. Partial Frequency Redistribution

Strong resonance lines are typically good indicators of chromospheric activity. They are characterized as optically thick lines with broad absorption wings that form in the photosphere and lower chromosphere with cores that form in the upper chromosphere and transition region. Since these lines dictate information regarding the thermodynamic properties of the stellar upper atmosphere and provide constraints on the Lyman continuum and EUV spectrum (Linsky et al. 2014; Shkolnik & Barman 2014), it is important to model these lines particularly well.

Complete frequency redistribution (CRD) accounts for overlapping radiative transitions and is generally a good approximation to use when calculating the majority of line profiles. In strong resonance lines, however, coherent scattering of photons largely affects the shape of the wings in the line profiles, requiring the inclusion of partial frequency redistribution (PRD) in the radiative transfer calculations.

As a part of Peacock et al. (2019), we added PRD capabilities to PHOENIX and demonstrated the importance of these calculations when computing the H I Ly $\alpha$  line in M stars. In this paper, we extend these calculations to additional strong resonance lines that are

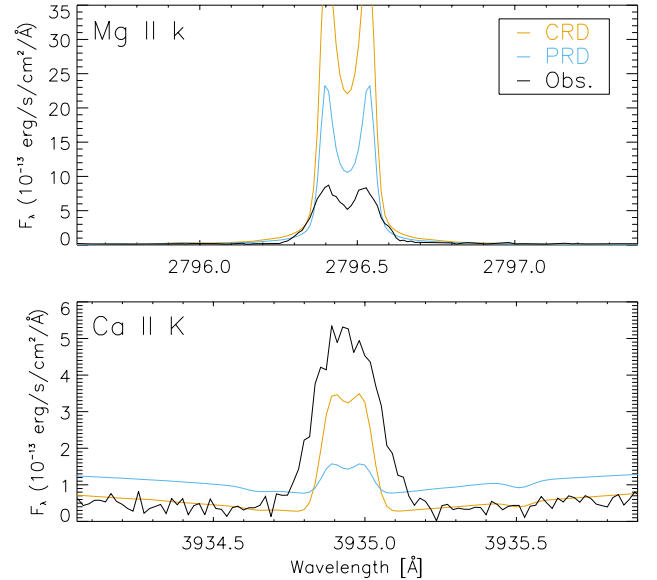


**Figure 2.** Computed non-LTE profiles for GJ 832 assuming CRD (orange) versus PRD (blue) for Mg II  $k$  (top panel) and Ca II K (bottom panel) compared to high resolution observed spectra (black; top panel: *HST* STIS (France et al. 2016), bottom: Keck/HIRES (Vogt 2011)).

commonly used as chromospheric diagnostics: Mg II  $h$  &  $k$  and Ca II H & K. In Figure 2, we show the impact of including the PRD formalism when computing the Mg II  $k$  and Ca II K line profiles in our model for GJ 832. When computed assuming CRD, the model Mg II  $k$  profile marginally overpredicts the wings and overpredicts the strength of the observed line core by a factor of  $\sim 13$ . Observations of Mg II, however, are contaminated by interstellar absorption, so direct comparisons to the line core cannot be drawn. Estimates suggest  $\sim 30\%$  attenuation of the intrinsic Mg II line core, affecting the line profiles from  $2796.4 - 2796.6 \text{ Å}$  and  $2803.6 - 2803.7 \text{ Å}$  (France et al. 2013) as compared to the nearly 100% interstellar absorption of the H I Ly $\alpha$  core (Youngblood et al. 2016). We find that the PRD calculations decrease the flux in the Mg II line peaks and line core by nearly a factor of two, with marginal effects on the strength of the wings.

The CRD Ca II K profile slightly underpredicts the observed profile, with the total line flux differing by a factor of 1.9. Computing Ca II in PRD increases the strength of the wings and decreases the total line flux by a factor of four. Since the PRD calculations worsen the agreement to the observations for Ca II, we use the CRD formalism in computing this species in our models.

The broad wings of Ly $\alpha$  extend far enough from the line center that using PRD to compute this line profile drastically alters the FUV pseudocontinuum and influ-

ences which set of model parameters produces the spectrum that most closely matches the observations. Conversely, computing Mg II and Ca II in PRD versus CRD results in negligible changes to the surrounding continuum, such that the special treatment of these lines does not have an effect on the choice of model that best reproduces the observations as a whole, and therefore does not effect the predicted EUV spectrum. In future work, we will explore a non-linear temperature rise in the chromosphere, in which the accuracy in modeling both Mg II and Ca II will play a more vital role in determining the structure.

### 3. TARGETS

There are few M stars that have observations in X-ray, UV, optical, and IR wavelengths. For this work, we modeled 3 M star planet hosts of different subtypes that have UV spectroscopic observations and estimates for EUV fluxes calculated from empirical scaling relationships with Ly $\alpha$  from the MUSCLES Treasury Survey program (France et al. 2016; Youngblood et al. 2016; Loyd et al. 2016) as well as *GALEX* UV photometric detections (Bianchi et al. 2011; Shkolnik & Barman 2014):

*GJ 832* is an M1.5 V star that hosts two planets: a 0.64  $M_{Jupiter}$  planet at a semi-major axis of 3.56 au and a 5.4  $M_{\oplus}$  super-Earth located in the canonical habitable zone (0.16 au) (Wittenmyer et al. 2014). Its age is uncertain, but a rotational period of  $45.7 \pm 9.3$  days (Suárez Mascareño et al. 2015) indicates that it has a kinematic age of at least 3.1 Gyr (Newton et al. 2016; West et al. 2015). *GJ 832* has also been previously modeled in Fontenla et al. (2016), allowing for the opportunity to directly compare the two synthetic EUV spectra.

*GJ 176* is a 3.62 Gyr (Sanz-Forcada et al. 2011) M2.5 V star that hosts an 8.3  $M_{\oplus}$  planet orbiting at 0.066 au (Butler et al. 2009; Forveille et al. 2009). Youngblood et al. (2016) calculated the column density of H I in the interstellar medium along the line of sight to *GJ 176* and found the value to be among the lowest column densities measured in their sample of 11 M and K dwarfs. In the event of a new EUV telescope, the smaller concentration of interstellar hydrogen in the direction of *GJ 176* suggests that it would be a favorable target for follow-up EUV observations.

*GJ 436* is a  $6_{-5}^{+4}$  Gyr (Torres 2007) M3.5 V. Ly $\alpha$  transit observations of its Neptune-sized planet (23  $M_{\oplus}$ , 0.287 au) discovered by Butler et al. 2004 show a 56% transit depth that is most likely caused by a large cloud of escaping hydrogen (Kulow et al. 2014; Ehrenreich et al. 2015). Since EUV radiation drives atmospheric escape, a synthetic stellar EUV spectrum is essential for understanding the star-planet interaction in this system.

The effective temperature ( $T_{eff}$ ) is a primary driver of spectral shape, especially affecting NUV and visible wavelengths in M stars. There is significant variance in the literature values of  $T_{eff}$  for each target in our sample. Effective temperatures for *GJ 832* range from 3472 K (Wittenmyer et al. 2014) – 3993 K (Gaia Collaboration et al. 2018), for *GJ 176* range from 3416 K (Loyd et al. 2016) – 3897 K (Gaia Collaboration et al. 2018), and for *GJ 436* range from 3281 K (Loyd et al. 2016) – 3660 K (Gaia Collaboration et al. 2018). We computed models with the range of literature values and calculated synthetic visible and near-IR photometry over the same wavelengths as the filter profiles for: HIP: BT, VT; Johnson: B, V, J, H, K; POSS-II: J, F, i; Gaia: G; 2MASS: J, H, Ks, SDSS: g, r, i. We normalized the fluxes and compared the values to all available photometric detections (not including upper limits) returned by the VizieR Photometry Viewer<sup>2</sup> for each star within a 5" search radius. We used a  $\chi^2$  test to identify the best fit models to the photometry and to select our operational  $T_{eff}$  for each star. The best fit models are shown in blue in Figure 3, along with the upper and lower end members. Our operational stellar parameters are listed in Table 3.

### 4. COMPARISON OF MODELS TO OBSERVATIONS

We calibrate our models to replicate *HST* COS and STIS observations taken as a part of the MUSCLES Treasury Survey (Version 2.1) France et al. (2016) and Keck High Resolution Echelle Spectrometer (HIRES) observations from Vogt (2011). We scale the high resolution ( $\Delta\lambda \sim 0.01$  Å) model spectra by  $R_*^2/d^2$  and account for radial velocity shifts, rotational broadening, and instrumental broadening before comparing to observations.

We determine the steepness of the temperature gradient in the transition region,  $\nabla T_{TR}$ , by fitting observations of emission lines with formation temperatures greater than 8,000 K (Si IV, He II, C IV, and N V). We use the FUV and NUV psuedocontinuum and the wings of Ly $\alpha$ , Mg II  $h$  &  $k$ , and Ca II H & K, which have formation temperatures below 8,000 K, to determine  $m_{Tmin}$  and  $m_{TR}$ . Best fits were determined by eye and with a  $\chi^2$  test using the mentioned diagnostic lines. As we are using a 1D simplified linear temperature structure to model a 3D object with spatially varying active regions, it is not expected that the models will reproduce all observed chromospheric lines well. A good match to the observed UV continuum and many emission lines that

<sup>2</sup> <http://vizier.u-strasbg.fr/vizier/sed/>

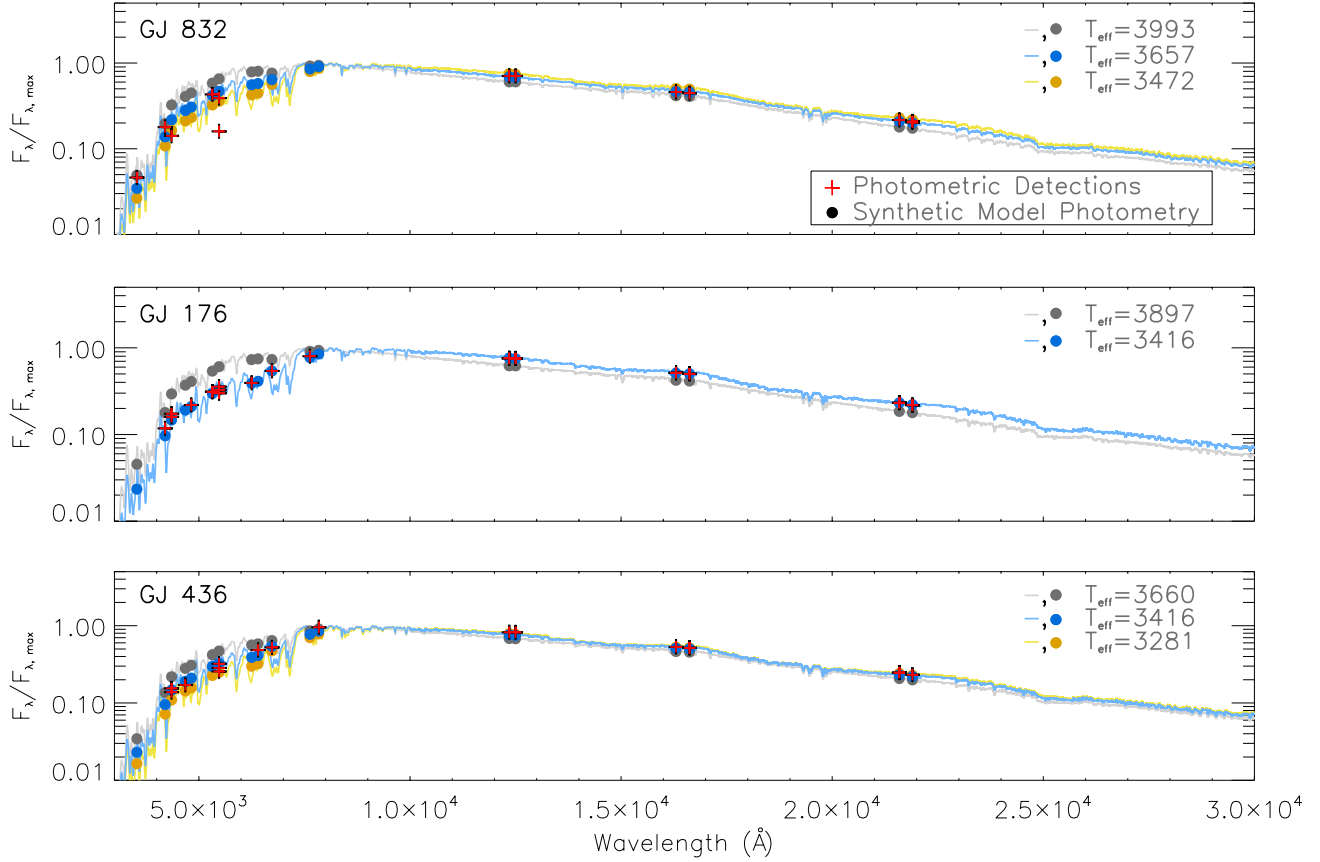


**Figure 3.** Flux-normalized PHOENIX synthetic spectra and synthetic photometry (circles) for the range of effective temperatures found in the literature (coldest: yellow, hottest: grey) compared to all available visible and near-IR photometric detections per star returned by the VizieR Photometry Viewer (red crosses). Best fit models are plotted in blue. Spectral resolution in the spectra has been degraded for clarity.

References for photometric detections –

GJ832: 1,2,3,4,5,6,7,8,9,10,11; GJ176: 1,2,3,4,5,6,8,9,10,11,12,13,14,15,16,17,18; GJ436: 1,2,3,5,8,9,10,12,13,15,16,19,20

References – (1) Cutri et al. 2003; (2) Röser et al. 2008; (3) Roeser et al. 2010; (4) Zacharias et al. 2012; (5) Neves et al. 2013; (6) Santos et al. 2013; (7) Bourges et al. 2014; (8) Gaidos et al. 2014; (9) Ward-Duong et al. 2015; (10) Altmann et al. 2017; (11) Schneider & Shkolnik 2018; (12) Soubiran et al. 2016; (13) Droege et al. 2006; (14) Huber et al. 2017; (15) Trifonov et al. 2018; (16) Terrien et al. 2015; (17) Ofek 2008; (18) Ammons et al. 2006; (19) Lasker et al. 2008; (20) Triaud et al. 2014

cover a broad range of formation temperatures is indicative that the simplified upper atmospheric temperature structure and predicted spectrum are a good general approximation for the star as a whole. The model parameters that best replicate the *HST* observations are given in Table 1.

#### 4.1. Visible Spectrum

The emission strengths of Ca II H (3968.17 Å) & K (3933.66 Å) and H $\alpha$  (6562.8 Å) are commonly used indicators of chromospheric activity found in the visible region of a stellar spectrum. H $\alpha$  is a commonly used diagnostic for solar-type stars since the nearby continuum emission is relatively weak and it typically has broad wings. However, for M type stars, H $\alpha$  can be a complicated diagnostic of chromospheric activity since

it progresses from presenting as an absorption feature to an emission feature with increasing activity (Gomes da Silva et al. 2011). The Ca II H & K doublet does not undergo the transition from absorption to emission, making it a more favorable diagnostic feature detectable from the ground. For example, while the H $\alpha$  absorption spectra for the stars in this study imply that they are optically inactive (Gizis et al. 2002), the strength of the Ca II H & K emission cores and observations of UV flares indicate that they do display chromospheric activity (Vogt 2011; Shkolnik & Barman 2014; France et al. 2016; Loyd et al. 2018b).

In M dwarfs, resonance lines of ions, including the Ca II doublet, have very weak wings because the photosphere and lower chromosphere are mostly neutral. The line cores of Ca II form in the upper chromosphere/lower



**Table 3.** Stellar Parameters

	GJ 832	GJ 176	GJ 436
Spectral Type ..	M1.5 <sup>1</sup>	M2.5 <sup>2</sup>	M3.5 <sup>3</sup>
Age (Gyr) .....	>3.1 <sup>4</sup>	3.62 <sup>5</sup>	6 <sup>+4</sup> <sub>-5</sub> <sup>6</sup>
$T_{eff}$ (K) .....	3657 <sup>1</sup>	3416 $\pm$ 100 <sup>7</sup>	3416 $\pm$ 100 <sup>8</sup>
$\log(g)$ (cm s <sup>-2</sup> ) ..	4.7 <sup>9</sup>	4.79 $\pm$ 0.13 <sup>10</sup>	4.84 $\pm$ 0.018 <sup>6</sup>
$M_*$ ( $M_\odot$ ) .....	0.45 $\pm$ 0.05 <sup>9</sup>	0.45 <sup>11</sup>	0.507 <sup>+0.071</sup> <sub>-0.062</sub> <sup>3</sup>
$R_*$ ( $R_\odot$ ) .....	0.499 $\pm$ 0.017 <sup>12</sup>	0.45 $\pm$ 0.02 <sup>11</sup>	0.455 $\pm$ 0.018 <sup>11</sup>
$[Fe/H]$ .....	-0.17 $\pm$ 0.09 <sup>13</sup>	-0.01 $\pm$ 0.09 <sup>13</sup>	-0.03 $\pm$ 0.09 <sup>13</sup>
$v \sin(i)$ (km s <sup>-1</sup> ) ..	...	<0.8 <sup>2</sup>	0.24 <sup>+0.38</sup> <sub>-0.17</sub> <sup>8</sup>
$v_{rad}$ (km s <sup>-1</sup> ) ...	12.52 $\pm$ 0.15 <sup>14</sup>	25.68 $\pm$ 0.29 <sup>14</sup>	9.6
Distance (pc) ...	4.965 $\pm$ 0.001 <sup>14</sup>	9.473 $\pm$ 0.006 <sup>14</sup>	9.755 $\pm$ 0.007 <sup>14</sup>

**References**—(1) Bailey et al. 2009; (2) Forveille et al. 2009; (3) von Braun et al. 2014; (4) Newton et al. 2016; (5) Sanz-Forcada et al. 2011; (6) Torres 2007; (7) Loyd et al. 2016; (8) Lanotte et al. 2014; (9) Wittenmyer et al. 2014; (10) Santos et al. 2013; (11) von Braun et al. 2014; (12) Houdebine 2010; (13) Neves et al. 2014; (14) Gaia Collaboration et al. 2018

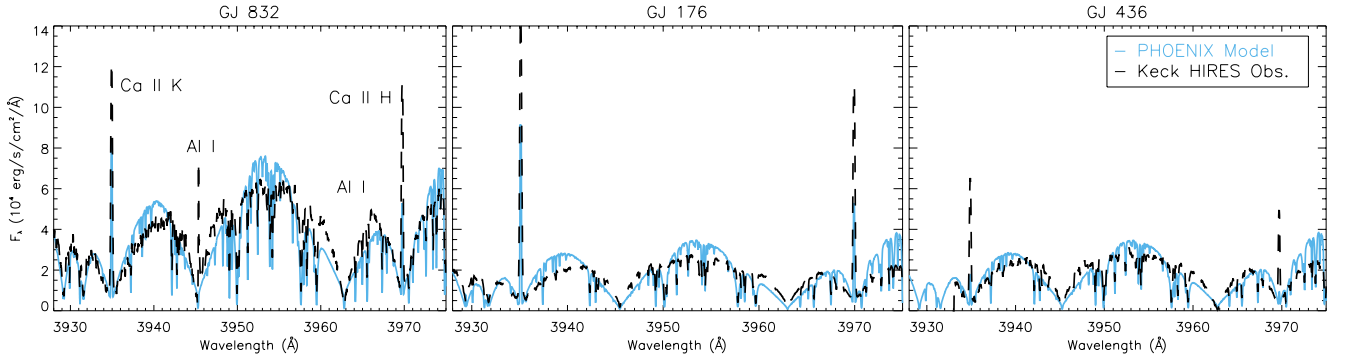


**Figure 4.** Comparison of the PHOENIX spectra (blue, solid) to Ca II H (3968.17 Å) & K (3933.66 Å) Keck/HIRES observations (black, dashed) (Vogt 2011). Observations are converted to vacuum wavelengths and scaled to the stellar surface. The resolution of the synthetic spectra has been reduced to that of the observations,  $\Delta\lambda = 0.05$  Å.

transition region between 5,000 and 20,000 K while the neighboring emission peaks form at cooler temperatures deeper in the atmosphere between 4,000 and 10,000 K. Since these lines yield information about the temperature structure, before stellar UV spectral observations were available, early semiempirical M dwarf chromosphere models were based on fitting ground-based Ca II K observations (Giampapa et al. 1982). More recently, Youngblood et al. (2017) found that the equivalent width of the Ca II K line could be used to estimate the stellar surface flux in several ultraviolet emission lines, including Ly $\alpha$ , and developed a scaling relationship to estimate EUV fluxes using time-averaged high resolution Ca II observations.

We compare our model spectra to Keck/HIRES observations of Ca II H & K from Vogt (2011) in Figure 4. Deviations of the synthetic spectra from the observations in the continuum surrounding the Ca II doublet

are related to the model parameter at the base of the chromosphere,  $m_{Tmin}$ . Adjusting  $m_{Tmin}$  to better fit this region of the spectrum worsens the agreement of the model to the NUV continuum and does not influence the EUV spectrum. For all three models, the far wings of the lines replicate the observations well, but the models underpredict the observed emission cores by 45 – 70%. We attribute uncertainties in our estimated Ca II lines to the lack of ambipolar diffusion in the model. Ambipolar diffusion is associated with coronal back-heating and is important for determining the hydrogen ionization near where the cores of Ca II H & K are forming ( $\sim 10,000$  K). In upcoming work, we will add a corona and ambipolar diffusion to our model and will explore how this physics affects the temperature at which hydrogen becomes fully ionized, which determines the onset of the transition region.

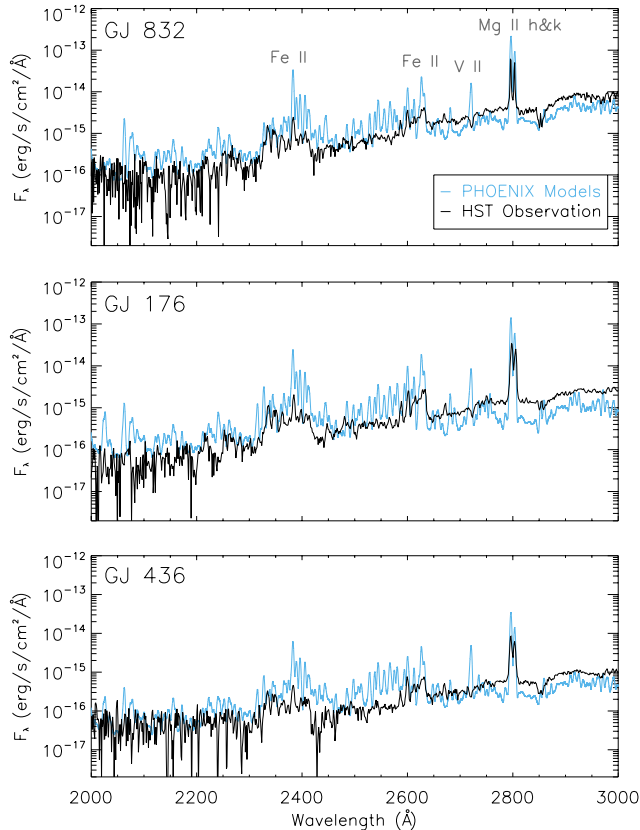


**Figure 5.** Near-UV PHOENIX spectra (blue) at the spectral resolution of the *HST* observations (black). Prominent emission features are labeled in the top panel. The *HST* observations for GJ 176 and GJ 436 were taken with the G230L grating on STIS, while the spectrum for GJ 832 is comprised of observations taken with the multiple gratings on both STIS and COS, including the high resolution grating used to measure Mg II.

#### 4.2. Near Ultraviolet Spectrum

At low resolution ( $\Delta\lambda \sim 3 \text{ \AA}$ ), the NUV spectrum is characterized by the Mg II *h* (2802.7  $\text{\AA}$ ) & *k* (2795.53  $\text{\AA}$ ) doublet and a forest of Fe II emission lines spanning 2300 – 2650  $\text{\AA}$ . The pseudo-continuum is shaped by molecular opacity sources, most importantly: NH, CH, OH, and H<sub>2</sub>. In Figure 5, we compare our synthetic spectra to *HST* observations taken as part of the MUSCLES Treasury survey. We find good general agreement in the pseudo-continuum for all three stars. From 2375 – 2630  $\text{\AA}$ , the pseudo-continuum is elevated by excess flux from OH and H<sub>2</sub> causing the models to overpredict the forest of Fe II lines. The models also overpredict a strong V II line at 2721  $\text{\AA}$ .

The Mg II *h* & *k* lines are diagnostics of the chromospheric thermal structure located in the NUV region. The line cores form at temperatures around 10,000 K,

the emission peaks at  $\sim 6,000 \text{ K}$ , and the wings near 3,000 – 4,000 K. This emission feature is similar to the Ca II H & K doublet in that both display weak wings, but the Mg II lines typically have stronger emission cores in M dwarfs. This is due to a higher abundance of Mg than Ca, a larger ionization potential of Mg+ than Ca+, and a weaker background photospheric spectrum at shorter wavelengths (Linsky 2017).

Observations of Mg II are contaminated by interstellar absorption, estimated to attenuate 30 – 35% of the intrinsic line flux (France et al. 2013). Additional absorption of Mg II lines has been observed in host stars during the transit of exoplanets with escaping atmospheres, such as WASP-12b, attributed to metals in the exospheric cloud (Fossati et al. 2010). It is therefore possible that the intrinsic Mg II emission profiles of GJ 436 are further attenuated by the escaping atmosphere of its warm Neptune mass planet. Due to the low resolution modes used on the G230L grating on COS and STIS, corrections were not done for Mg II for any of the *HST* observations (France et al. 2016). Calculated line fluxes for Mg II *h* & *k* for the models and observations are given in Table 4. The spectral resolution of the models was reduced to that of the observations before calculating the line fluxes. We have also increased the observed line fluxes by 30% in order to make a more accurate comparison to the intrinsic stellar values, and find that our model predictions are within a factor of 1.5 of the corrected Mg II fluxes for GJ 176 and GJ 436, and within a factor of  $\sim 7$  for GJ 832.

#### 4.3. Far Ultraviolet Spectrum

In Figure 6, we compare our synthetic FUV spectra to the MUSCLES composite *HST* observations. We find good general agreement with the FUV continuum, which is shaped by recombination edges of Si, Mg, and Fe.

The FUV spectrum is populated with emission lines that form in both the chromosphere and transition region, including H I, N V, C I, II & IV, O II & IV, and Si IV (labeled in the top panel of Figure 6). Individual emission line profiles for H I Ly $\alpha$ , N V, C IV, and Al II as compared to the observations are shown in Figure 7. Calculated emission line fluxes from both the models and observations are given in Table 4. The models reproduce H I Ly $\alpha$ , Si III, O IV, the N V doublet, and the C IV line at 1551  $\text{\AA}$  within a factor of 2.5 of the observations. However, due to the simplified linear temperature structure, not all chromospheric lines are fit well. The models underpredict Si IV, O II, and the C IV line at 1548  $\text{\AA}$  by an order of magnitude. This implies that some EUV emission lines that form at similar temperatures in the lower transition region may also be

**Table 4.** Line fluxes ( $\text{erg cm}^{-2} \text{ s}^{-1}$ ) of select chromosphere and transition region lines

Species	$\lambda$ (Å)	GJ 832		GJ 176		GJ 436	
		Model	<i>HST</i>	Model	<i>HST</i>	Model	<i>HST</i>
Si III	1206.51	9.76	24.76	17.05	40.24	45.25	49.87
H I (Ly $\alpha$ ) <sup>a</sup>	1215.67	4033.81	6602.65	1438.29	3656.67	2976.69	5906.28
N V	1238.82	63.08	56.23	68.53	69.77	110.13	46.47
N V	1242.81	34.61	29.12	36.01	36.18	57.04	23.62
C II <sup>b</sup>	1334.53	29.59	26.63	5.55	22.97	5.06	9.04
C II <sup>b</sup>	1337.71	59.24	46.27	14.38	70.36	16.39	24.43
Si IV	1393.76	5.64	56.37	2.01	48.19	1.26	11.82
O IV	1401.16	3.48	5.11	1.34	3.92	1.41	1.51
Si IV	1402.77	10.27	31.4	2.45	23.04	2.42	7.27
C IV	1548.19	9.87	65.70	7.50	171.18	8.96	144.40
C IV	1550.77	41.54	32.87	25.38	89.63	42.93	69.86
O II	1639.77	5.45	140.54	4.11	142.39	4.91	67.65
Al II	1670.79	247.25	42.98	144.79	38.09	119.68	21.91
Mg II <i>k</i> <sup>b</sup>	2796.35	317.10	43.462	203.84	124.97	126.26	84.43
Mg II <i>h</i> <sup>b</sup>	2803.53	138.58	29.143	84.05	88.66	88.5	57.77

NOTE—Computed and observed emission line fluxes at the stellar surface and continuum normalized. *HST* fluxes are calculated from the MUSCLES v2.1 panchromatic spectral energy distributions that maintain the native instrument resolutions and have been scaled by  $d^2/R_{star}^2$ .<sup>a</sup>Observed Ly $\alpha$  fluxes are calculated using the reconstructed profile from Youngblood et al. (2016).<sup>b</sup>Observed emission line fluxes have been corrected for an estimated 30% absorption by interstellar Mg II and C II.

underpredicted. The agreement between the synthetic spectra and each of the aforementioned lines can be improved by decreasing the temperature gradient in the transition region and reducing the thickness of the chromosphere. Making these adjustments, however, worsens the agreement with other FUV emission lines and elevates the EUV – FUV pseudocontinuum by up to an order of magnitude. Since our final spectra are a good match to the observed UV continuum and many emission lines that form at temperatures found across the entire upper atmosphere, we conclude that the simplified temperature structures and predicted EUV spectra are good general approximations for each star.

The strongest emission line in the FUV spectrum is the Ly $\alpha$  resonance line. For most M dwarfs, it contributes up to 75% of the total flux in the FUV region (France et al. 2013). Unfortunately, observations of the Ly $\alpha$  line for any star other than the Sun are heavily contaminated by both geocoronal airglow and interstellar hydrogen absorbing nearly all of the line core. In order to determine the intrinsic stellar line profile, observations must be reconstructed using interstellar parameters along the line of sight to the star (Wood et al.

2005; France et al. 2013; Youngblood et al. 2016). In the top panels of Figure 7, we show both the raw *HST* observations and the Youngblood et al. (2016) reconstructions. Our models closely reproduce the wings of Ly $\alpha$  in the raw *HST* observation, but present with a self reversed core that results in calculated Ly $\alpha$  line fluxes  $1.6 - 2.5 \times$  less than the reconstructed profiles. While the absorption in the raw *HST* observations is due to contamination, the central reversal in our models is a direct result of non-LTE effects.

In the ultraviolet spectrum, non-LTE effects become important as the source function deviates from the Planck function in both the chromosphere and transition region. When allowing for departures from LTE, optically thick lines that form at various depths in a stellar atmosphere (e.g. Ly $\alpha$ , Mg II, Ca II) can present in emission with a self-reversed core. Observations of the Sun in both active and quiescent states show self-reversals in Ly $\alpha$ , Mg II *h* & *k*, and Ca II H & K lines (Linsky & Avrett 1970; Fontenla et al. 1988; Staath & Lemaire 1995; Tian et al. 2009). In M dwarf stars, inverted cores are observed in high resolution measurements of Mg II

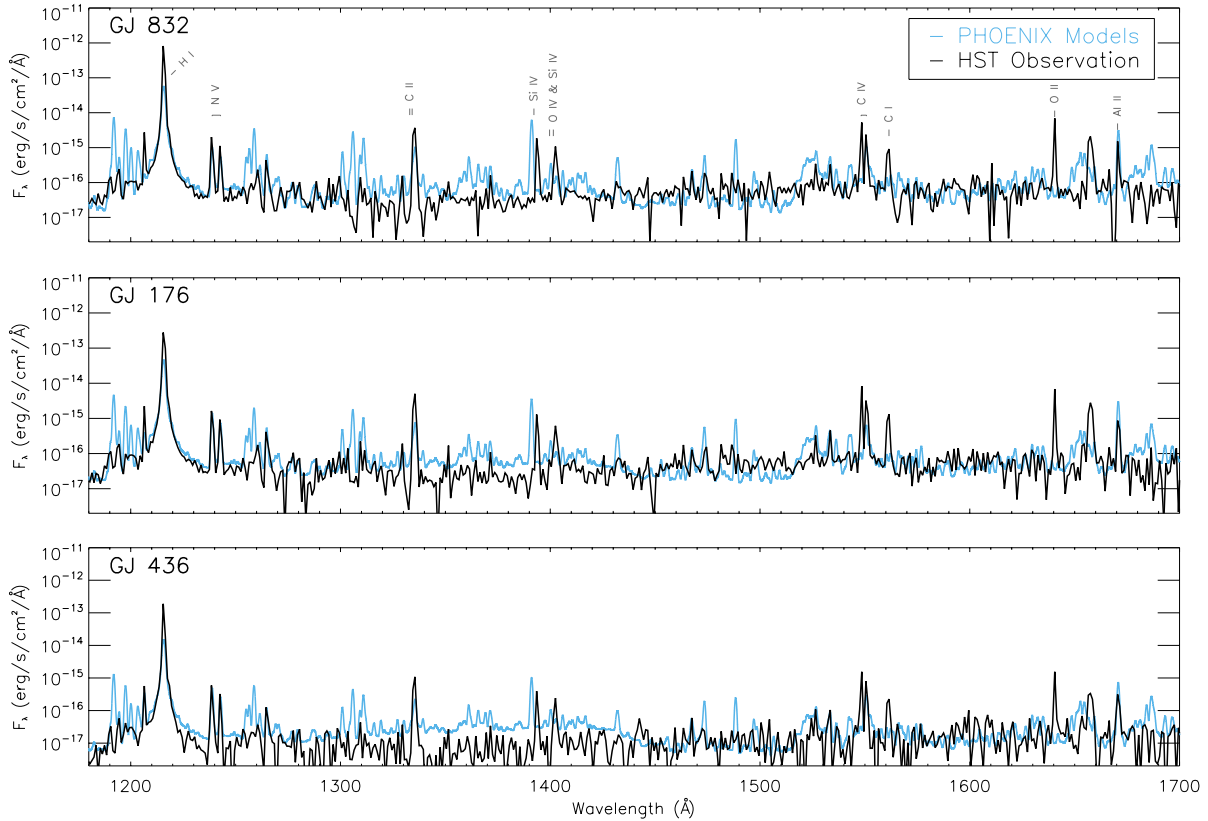


**Figure 6.** Comparison of the far-UV PHOENIX spectra (blue) to the MUSCLES composite *HST* spectra (black). Both spectra are convolved to a resolution of 1 Å. Prominent emission features are indicated in the top panel.

*h* & *k* (France et al. 2013) and some Ca II H & K lines (Rauscher & Marcy 2006).

While Mg II *h* & *k* form at slightly cooler temperatures than Ly $\alpha$ , they have similar line profiles in the observed solar spectrum (Donnelly et al. 1994; Lemaire et al. 1998). Due to their similarities in the Sun, observations of the Mg II doublet have been used to estimate the shape of the central portion of the Ly $\alpha$  profile for M stars after fitting the ISM absorption (Wood et al. 2005). Low instrument resolution, however, can mask the existence of an inverted core in Mg II lines. For example, in Wood et al. (2005), *HST* observations of Mg II *h* & *k* and the corresponding best fit Ly $\alpha$  profiles for five M stars do not include a central reversal, but when utilizing a high resolution grating, observations of GJ 832 from France et al. 2013 do show a central reversal in Mg II (Figure 2).

Contamination of the stellar Ly $\alpha$  emission line from the geocoronal feature can be circumvented if observing a high radial velocity target. For example, the M1 star, Kapteyn’s Star, has a radial velocity ( $V = +245 \text{ km s}^{-1}$ ) such that Ly $\alpha$  is Doppler shifted 0.99 Å away from the geocoronal contribution. Guinan et al. (2016) obtained high resolution *HST* observations of the Ly $\alpha$  region of Kapteyn’s Star and determined the stellar emission pro-

file presented with a faint self-reversal in the line core. Analysis of the same spectrum by Youngblood et al. (2016), however, fit the line with a Gaussian-shaped profile with no self-reversal. Additional high resolution observations of Ly $\alpha$  from high radial velocity M stars (e.g. A. Schneider et al., in prep.) as well as high resolution Mg II observations would help determine the actual Ly $\alpha$  line profile and intrinsic flux from M stars.

Modeling efforts by Fontenla et al. (2016) also predict inverted cores in both the Mg II doublet and Ly $\alpha$  for GJ 832. The smaller depths of the central reversal in the Kapteyn’s Star observation and the Fontenla et al. (2016) model lead us to believe our models could be underpredicting the flux in the core of Ly $\alpha$  by up to 40% if the intrinsic profile does not contain any central reversal. We attribute uncertainty in the model Ly $\alpha$  line profiles to the parameterization in the transition region and the lack of ambipolar diffusion and a corona in our model. Peacock et al. (2019) found that this reversal is very sensitive to  $\nabla T_{TR}$ , with less steep temperature gradients resulting in shallower reversals in the Ly $\alpha$  profile. As mentioned in Section 4.1, the base of the transition region is determined by where hydrogen becomes fully ionized. Adding a corona above the transition region leads to back irradiation from the  $10^6 \text{ K}$  plasma, pho-

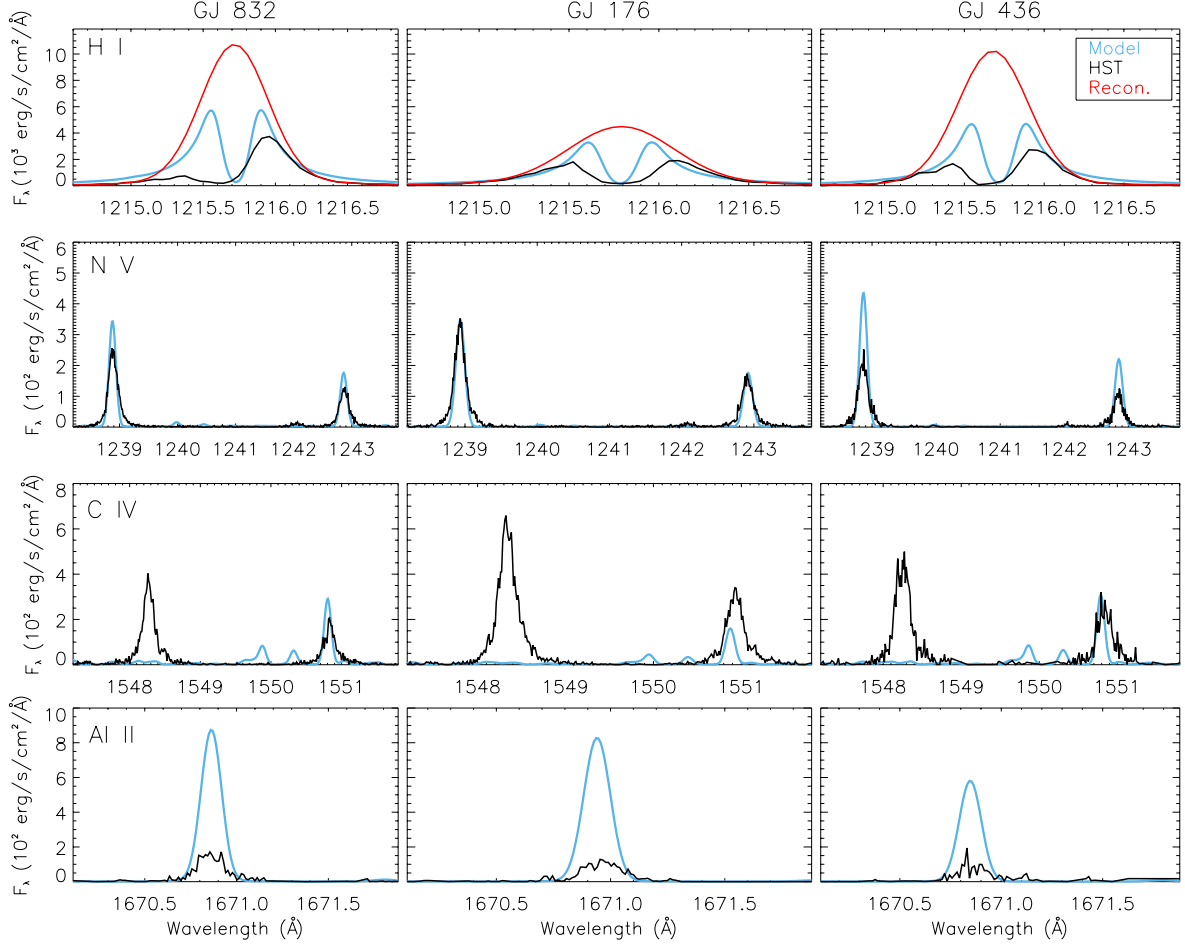


**Figure 7.** Select FUV emission line profiles from the PHOENIX spectra (blue) compared to *HST* spectra (black) continuum normalized and scaled to the surface of the star. In the top panels, the raw H I Ly $\alpha$  observation (black) is contaminated by interstellar absorption. The reconstructed profiles from Youngblood et al. 2016 are plotted in red. The central reversal in the model Ly $\alpha$  profiles are a result of non-LTE effects. The suppression of the C IV ( $\sim 1548$  Å) line is a result of the linear parameterization in the transition region ( $\nabla T_{TR}$ ,  $m_{TR}$ ), as the C IV lines form at slightly different temperatures found near the top of the chromosphere and base of the transition region.

toionizing the lower layers through ambipolar diffusion and affecting the collisional rates where the core is forming.

#### 4.4. Near UV and Far UV Photometry

Existing *GALEX* FUV (1340–1811 Å) and NUV (1687–3008 Å) detections of the stars measured using the elliptical Kron aperture are presented in Table 5. We compute synthetic photometry for the models over the same wavelength ranges as the *GALEX* FUV and NUV filter profiles and find that the calculated values match the FUV detections, but exceed the NUV due to the overestimated Fe II lines from 2375 – 2630 Å. We also note that M stars are UV active and the *GALEX* and *HST* observations were not taken contemporaneously. It is therefore not necessarily expected that the model that best reproduces the *HST* data also match the *GALEX* photometry within uncertainty.

Model  $F_{FUV}$  and  $F_{NUV}$  for GJ 832 are  $2.06 \times 10^{-16}$  erg cm $^{-2}$  s $^{-1}$  Å and  $12.41 \times 10^{-16}$  erg cm $^{-2}$  s $^{-1}$  Å, respectively, falling within the uncertainty of the FUV detection but overpredicting the  $F_{NUV}$  by a factor of 1.3. For GJ 176,  $F_{FUV} = 1.81 \times 10^{-16}$  erg cm $^{-2}$  s $^{-1}$  Å and  $F_{NUV} = 11.09 \times 10^{-16}$  erg cm $^{-2}$  s $^{-1}$  Å, matching the measured  $F_{FUV}$  and overpredicting the  $F_{NUV}$  detection by a factor of 1.7. Our model for GJ 436 overpredicts the singular  $F_{NUV}$  detection by a factor of 2.6,  $F_{NUV} = 3.05 \times 10^{-16}$  erg cm $^{-2}$  s $^{-1}$  Å (Table 5). We plot this information in Figure 8.

The three prescribed parameters designating the temperature structure in the chromosphere and transition region for the three stars are nearly the same (Table 1). As a result of this degeneracy, the UV continuum slope in the models are very similar:  $F_{NUV,G}/F_{FUV,G} = 5 - 6$ . Calculating this ratio with the *GALEX* detections



**Table 5.** Band integrated UV flux densities in ( $10^{-16}$  erg cm $^{-2}$  s $^{-1}$  Å $^{-1}$ )

	GALEX Detections		Models		
	$F_{FUV}$	$F_{NUV}$	$F_{EUV}$	$F_{FUV}$	$F_{NUV}$
GJ 832	$2.43 \pm 0.37$	$9.25 \pm 0.31$	14.74	2.06	12.41
GJ 176	$1.62 \pm 0.52$	$6.22 \pm 0.30$	17.04	1.81	11.09
GJ 436	...	$1.12 \pm 0.20$	6.06	0.60	3.05

NOTE—GALEX FUV and NUV photometric detections measured using the Kron aperture. Synthetic photometry from the PHOENIX models is calculated over  $\lambda_{EUV} = 100\text{--}1170$  Å and the same wavelengths as the GALEX FUV ( $\lambda_{FUV} = 1340\text{--}1811$  Å) and NUV ( $\lambda_{NUV} = 1687\text{--}3008$  Å) filter profiles.

for GJ 832 and GJ 176 both yield a ratio of  $\sim 4$ , supporting the plausibility that the upper atmospheres for these stars are likely analogous.

## 5. EXTREME ULTRAVIOLET SPECTRUM

Many emission features in the EUV (100 – 1170 Å) spectrum form in the upper chromosphere and transition region (e.g. He I (584 Å,  $10^{4.65}$  K) O V (629.7 Å,  $10^{5.3}$  K), and H I Ly $\beta$  (1025.7 Å,  $10^{4.5}$  K) (Sim & Jordan 2005)), with highly ionized lines forming in the corona (e.g. Fe IX (171 Å,  $10^6$  K) (Del Zanna et al. 2014)). Continuum emission forms in the chromosphere and includes contributions from the H I Lyman, He I and He II continua.

Our synthetic EUV spectra are presented in full resolution ( $\Delta\lambda < 0.1$  Å) in Figure 9 with noticeable bound-free edges of H I (912 Å), He I (504 Å), N II (418 Å), K II (392 Å), O II (353 Å), He II (228 Å). In addition to the many non-LTE emission features, also prominent are narrow, but very bright emission features for species not included in the non-LTE set: Fe VII (246 Å), Ne IV (402 Å), Ca V (558 Å) and O VI (1031, 1038 Å). The strength of the lines computed in the LTE, particularly those near 400 Å and 550 Å and the O VI lines near 1030 Å are likely overpredicted by up to a factor of ten. On account of these lines, we suggest that the fluxes in the 400 – 600 Å and 1000 – 1050 Å regions be taken as upper limits.

The current models do not include a corona, and therefore underpredict the flux from lines that form at temperatures greater than  $2 \times 10^5$  K. While the continuum and many EUV emission lines found between 200 – 1170 Å form below this temperature, the 100 – 200 Å wavelength range in the EUVE spectrum of the M2 flare star, AU Mic, is filled with Fe XIX – XXIII and Cr

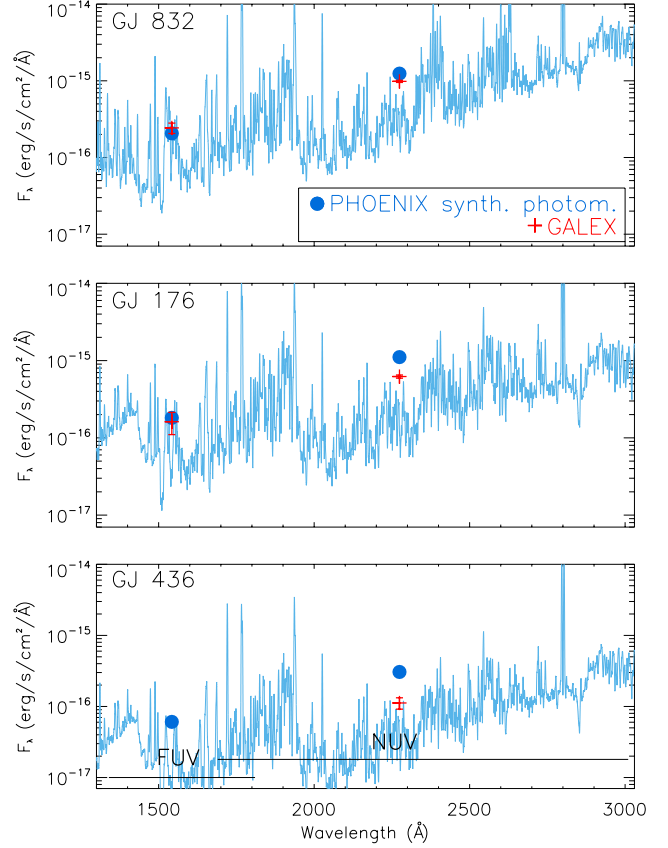


**Figure 8.** PHOENIX FUV–NUV spectra (blue) compared to GALEX photometry (red, crosses), with calculated synthetic photometry over the same wavelengths as the GALEX filter profiles plotted as blue circles. These wavelength ranges are indicated in the bottom panel. Values for the GALEX detections are listed in Table 5.

XVIII – XXI lines which form at coronal temperatures (Monsignori Fossi et al. 1996).

As a test to quantify the amount of EUV flux our synthetic spectra could be underestimating, we compared our models to versions with example coronal spectra added to them. We computed coronal spectra of AU Mic (high activity) and the quiet Sun (low activity) with CHIANTI version 9.0 (Dere et al. 2019), using the Differential Emission Measures (DEMs) of both objects from the CHIANTI database (Del Zanna et al. 2002). We truncated the temperature minimums at  $2 \times 10^5$  K so that there was no duplication of the PHOENIX model structures. We scaled the computed AU Mic spectrum and the quiet Sun spectrum to GJ 832, GJ 436, and GJ 176, and added the CHIANTI spectra to each PHOENIX spectrum. AU Mic is an active young M star (12 Myr) with elevated levels of FUV and NUV emission (Robinson et al. 2001), and likely emits more EUV flux than GJ 832, GJ 436, and GJ 176. The addition of a scaled AU Mic coronal spectrum to our models

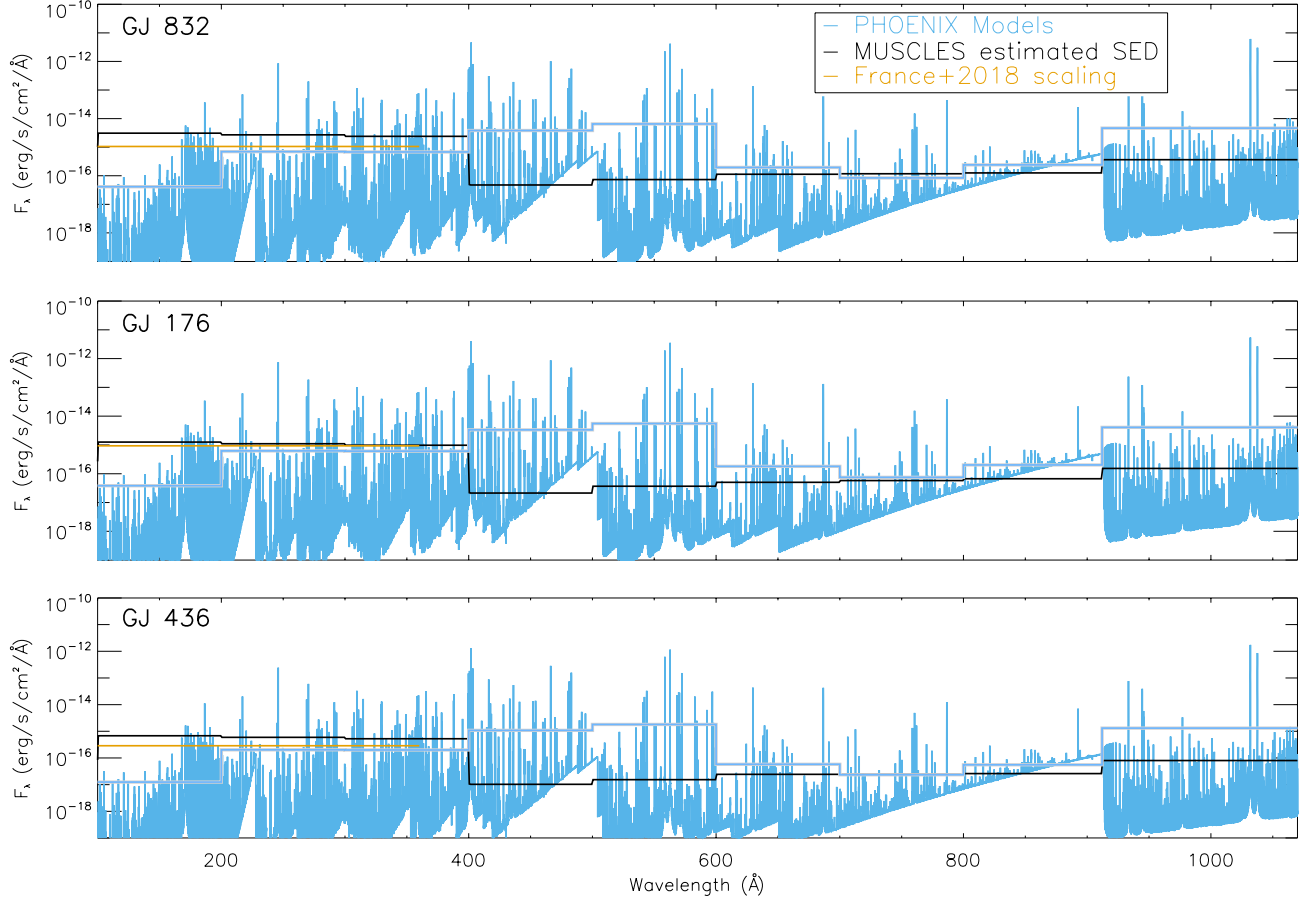


**Figure 9.** Full resolution EUV synthetic spectra and corresponding average flux densities in 100 Å wavelength bands (blue). Estimated EUV flux densities in 100 Å wavelength bands calculated using  $F_{EUV}/F_{Ly\alpha}$  scaling relationships from Linsky et al. (2014) in the MUSCLES SEDs are overplotted in black.  $F_{EUV}$  estimates from France et al. (2018) are overplotted in orange.

increases the EUV flux in the 100 – 200 Å region by a factor of 60, but only slightly impacts on the rest of the EUV spectrum, increasing the integrated flux over 100 Å wavelength bands by factors of 1 – 5. Adding the scaled coronal spectrum of the quiet Sun to our models changes the EUV flux in each wavelength band by less than a factor of two, except in the 100 – 200 Å band, which increases by a factor of five. Integrating over 100 – 1170 Å, the coronal flux contribution from either DEM increases the overall EUV flux by 4 – 45%. Without the flux contribution from coronal lines, our models underpredict the EUV spectrum at  $< 200$  Å by less than two orders of magnitude and by less than a factor of five at wavelengths  $> 200$  Å. In a future paper, we will incorporate both a corona and the associated ambipolar diffusion to our models, exploring temperature structures tailored for the field age M stars.

## 6. DISCUSSION

Since most of the EUV spectrum is unobservable due to interstellar contamination, there are no observations

of the stars in this study to directly compare our synthetic spectra against. Here, we compare our models to existing EUV estimates for the target stars calculated with empirical scaling relationships or semiempirical stellar models and discuss the uncertainties associated with each method:

### 6.1. Comparison of PHOENIX EUV Spectra to EUV Empirical Scaling Relationships

In the MUSCLES spectral energy distributions (SEDs), Youngblood et al. (2016) calculated the EUV spectrum for each star using  $Ly\alpha$  reconstructions in an  $F_{EUV}/F_{Ly\alpha}$  scaling relationship from Linsky et al. (2014). This method predicts the EUV flux from 100 – 1070 Å in 100 Å wavelength bands and is derived from a combination of observations and models. The scalings for wavelengths  $< 400$  Å are calculated from *EUVE* observations of M stars, while those from 912 – 1170 Å are determined from *FUSE* observations of K5 – M5 stars. The relationships for wavelengths between 400 – 912 Å are computed from the Fontenla (2013) solar

models and may not be appropriate for M stars. To compute the EUV flux using this scaling relationship, observations of the Ly $\alpha$  line must be reconstructed, contributing additional uncertainty to the predicted values. The  $F_{EUV}/F_{Ly\alpha}$  estimated SEDs are plotted in black in Figure 9 and have an estimated accuracy of  $\sim 20\%$  (Youngblood et al. 2016). For ease of comparison, we have overplotted the average flux densities for our models in 100 Å wavelength bands in blue. We find that this method is generally consistent with the synthetic spectra from 200 – 400 Å and 600 – 900 Å with fluxes agreeing within 40% in these regions.

France et al. (2018) used *EUVE* and *HST* spectra of 104 F–M stars to develop a scaling relationship for  $F(90 - 360 \text{ Å})$  based on N V or Si IV observations. While the FUV emission lines used in this relationship do not rely on reconstructions, uncertainties in correcting for the ISM absorption in the *EUVE* spectra and difficulties in measuring the continuum flux at these wavelengths result in uncertainties in the predicted EUV flux. The EUV fluxes for the target stars calculated with this scaling relationship are plotted in orange in Figure 9 and are estimated to be accurate within a factor of two. Comparing the France et al. (2018) scaling to the models across the full 90 – 360 Å range, the fluxes agree within factors of 0.95 – 2.2.

We also compare our model for GJ 436 to an EUV flux calculated in an  $F_{EUV}/F_X$  scaling relationship derived in Chadney et al. (2015). This scaling is derived from averaged solar EUV and X-ray observations taken daily over an 11 year period and estimates an EUV flux for 124 – 912 Å. Ehrenreich et al. (2015) calculated  $F_{EUV} = 2.34 \times 10^{-13} \text{ erg cm}^{-2} \text{ s}^{-1}$  for GJ 436 using X-ray observations of the star. The Linsky et al. (2014) Ly $\alpha$  scaling relationship is also derived from solar EUV observations, and yields a similar  $F(124 - 912 \text{ Å}) = 2.1 \times 10^{-13} \text{ erg cm}^{-2} \text{ s}^{-1}$  (Youngblood et al. 2016). Calculating the flux across the same wavelengths for our synthetic spectrum for GJ 436 yields a twice larger value of  $F_{EUV} = 4.34 \times 10^{-13} \text{ erg cm}^{-2} \text{ s}^{-1}$ .

Empirical scaling relationships allow for general estimates of the unobservable EUV flux using observations from accessible wavelengths, but are derived using either observations of the Sun or from a wide range of spectral types. They are hindered by uncertainties in measuring the ISM absorption as well as noncontemporaneous observations at wavelengths known to display significant variability. They are further limited in both wavelength resolution and versatility. Conversely, semiempirical stellar models can predict realistic EUV spectra at the high resolution needed for detailed studies of the photochemistry and escape in exoplanet atmo-

spheres and have the versatility to be used for a range of spectral type and activity state.

## 6.2. Comparison of PHOENIX and Solar-Stellar Radiation Physical Modeling tools GJ 832 Models

Fontenla et al. (2016) adapted their 1D non-LTE semiempirical solar atmosphere model (SRPM) (Fontenla et al. 2015) that reproduces observations of the Sun, including UV spectra, to compute the stellar spectrum of GJ 832 using their Solar-Stellar Radiation Physical Modeling (SSRPM) tools. Similar to PHOENIX, their models are comprised of a modified thermal structure in the upper atmosphere added to an initial photospheric model with similar luminosity and spectral type as GJ 832. The temperature-pressure profile is based on their SRPM model and is divided into a chromosphere and lower transition region computed in a plane-parallel approximation and an upper transition region and coronal model computed in a spherically-symmetric approximation. The coronal SSRPM model extends to hotter temperatures than our PHOENIX model (0.2 MK), to their maximum coronal temperature peaking at 2.7 MK.

In both the PHOENIX and SSRPM models, solar elemental abundances are assumed, and the calculations include several species in full non-LTE radiative transfer in addition to millions of effectively thin background atomic and molecular lines. In our PHOENIX model, we consider 73 atoms and ions in full non-LTE, compared to 55 species (including H<sup>+</sup> and H<sub>2</sub>) in the Fontenla et al. (2016) SSRPM model.

We compare the thermal structure of our GJ 832 model to the lower transition region, chromosphere and photosphere profile for the SSRPM GJ 832 model in Figure 10. The GJ 832 models are both qualitatively and quantitatively very similar in the photosphere, but the chromospheric structure and onset of the thermally unstable transition region differ. The thermal structure in the SSRPM model has a steep temperature rise in the lower chromosphere near  $P_{gas} \approx 15 \text{ dynes cm}^{-2}$  followed by a near-constant temperature plateau in the upper chromosphere similar to their solar model. The temperature plateau results from the balance of radiative losses with non-radiative heating, and is where singly ionized metals are the dominant stages of ionization (Linsky 2017). Our model employs a linear temperature rise in  $\log(\text{column mass})$  for all chromospheric layers, which corresponds to a linear rise in  $\log(P_{gas})$  for this model, and similarly begins near  $P_{gas} \approx 15 \text{ dyne cm}^{-2}$ .

As described in Section 4, the Mg II doublet is an important diagnostic for the thermal profile in the chromosphere. We compare our PHOENIX model Mg II *h* & *k* profiles to the SSRPM model profiles, and the high res-

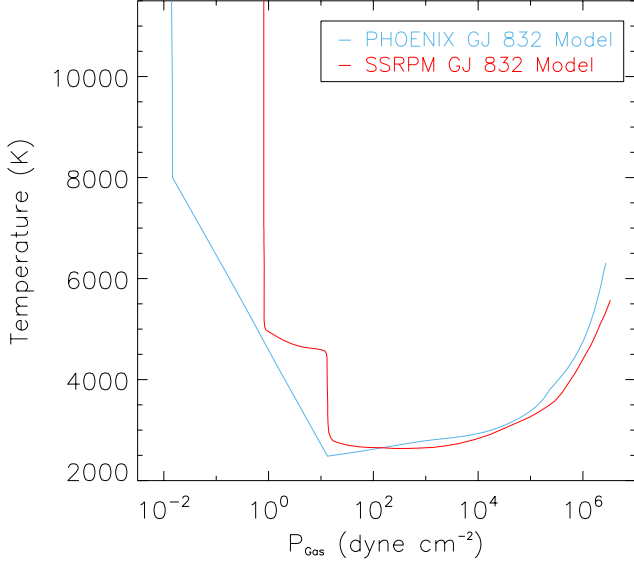


**Figure 10.** Temperature vs. gas pressure distributions in the lower transition region, chromosphere, and photosphere for the PHOENIX (blue) and the Fontenla et al. (2016) SSRPM (red) GJ 832 models. The upper transition region in the PHOENIX model extends to  $2 \times 10^5$  K. The final SSRPM GJ 832 model structure is coadded with a coronal temperature distribution that peaks around  $2.7 \times 10^6$  K.

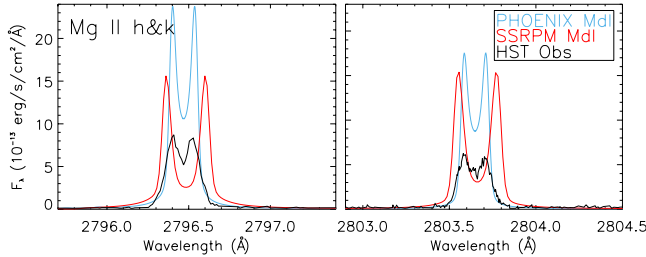


**Figure 11.** Mg II *h* & *k* profiles from the PHOENIX (blue) and SSRPM (red) models of GJ 832 compared to the high resolution STIS E230H observation (black). The observations have not been corrected for interstellar absorption.

olution STIS E230H observations from the MUSCLES SED in Figure 11. Both models display central reversals due to non-LTE effects. Since the observed profiles have not been corrected for interstellar absorption a direct comparison to the core of the lines cannot be confidently made. The PHOENIX model computed in PRD more closely reproduces the observed line width than the SSRPM model. The wings of Mg II begin forming around 3,000 K, indicating that the lower chromosphere may have a shallower slope than predicted in the SSRPM model.

Above the chromosphere, both models simulate a transition region with a steep temperature gradient governed by matching emission lines in the observed FUV

spectrum. In our model, we set the temperature at the base of the transition region to 8,000 K, based on when the dominant cooling agent, neutral hydrogen, becomes fully ionized. In the SSRPM model, the transition region begins at 5,000 K. The likely reason for this discrepancy is the inclusion of a corona and ambipolar diffusion in the SSRPM tools, which are not yet included in PHOENIX. Using their solar model, Fontenla et al. (1990) analyzed the energy balance of radiative losses with the downward flow of conductive heat and hydrogen ionization energy due to ambipolar diffusion from the corona. The authors found that the radiative losses were mainly due to hydrogen, and that ambipolar diffusion is greatly important in determining the hydrogen ionization in the lower transition region.

Figure 12 shows the PHOENIX and SSRPM synthetic EUV – NUV spectra compared to the MUSCLES SED for GJ 832. We find good general agreement between all spectra long-ward of 200 Å. The SSRPM EUV spectrum from 100 – 912 Å is comprised of 36.4% emission from the chromosphere and lower transition region model, and 63.3% emission from the upper transition region and corona model. As compared to the SSRPM model, we estimate that the lack of coronal flux in our PHOENIX model may contribute up to an 80% under-prediction in only the 100 – 200 Å range. While the maximum temperature in our model does not extend to the same  $\sim 10^6$  K coronal temperatures, we find that the EUV spectrum from 200 – 1170 Å compares well to the SSRPM model, with  $F(\lambda_{200-1170} \text{ Å}) = 1 \times 10^{-12} \text{ erg cm}^{-2} \text{ s}^{-1}$  for our model compared to  $F(\lambda_{200-1170} \text{ Å}) = 4 \times 10^{-13} \text{ erg cm}^{-2} \text{ s}^{-1}$  for that from Fontenla et al. (2016).

Integrating over 100 – 912 Å, we find close agreement between our computed EUV luminosity:  $\log L_{\text{EUV}} = 27.31 \text{ erg s}^{-1}$ , with the SSRPM model:  $\log L_{\text{EUV}} = 27.26 \text{ erg s}^{-1}$  and two other methods described in Fontenla et al. (2016). Sanz-Forcada et al. (2011) calculated a predicted EUV luminosity for GJ 832 using *ROSAT* X-ray observations. These observations give an  $L_X$  3.3 times higher than *XMM-Newton* observations, indicating increased activity during the *ROSAT* measurement. Fontenla et al. (2016) scaled the predicted luminosity from Sanz-Forcada et al. (2011) by this factor of 3.3 to yield  $\log L_{\text{EUV}} = 27.38 \text{ erg s}^{-1}$ . Finally, the calculated EUV luminosity from the  $F_{\text{EUV}}/F_{\text{Ly}\alpha}$  derived spectrum in the MUSCLES SED is  $\log L_{\text{EUV}} = 27.39 \text{ erg s}^{-1}$ . The similarities of the predicted EUV luminosities for this star using a variety of methods and observations gives us confidence that all four techniques can be used to estimate the broadband EUV flux, however, the semiem-



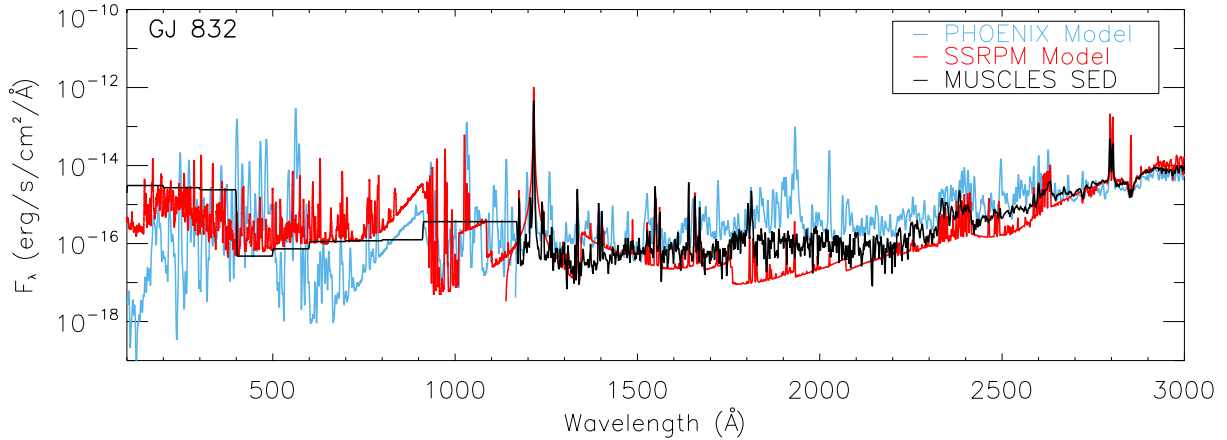


**Figure 12.** Comparison of EUV-NUV spectra for GJ 832. The PHOENIX model spectrum (blue) and Fontenla et al. (2016) SSRPM model spectrum (red) have been degraded to the same 1 Å resolution as the MUSCLES SED (black).

pirical models will provide the fine spectral resolution necessary for detailed studies of exoplanet atmospheres.

## 7. CONCLUSIONS

We present high resolution EUV – IR synthetic spectra of three early M planet hosts: GJ 832, GJ 176, and GJ 436. These synthetic spectra reproduce UV and visible spectral observations and UV, visible, and near-IR photometric detections and predict EUV fluxes similar to the active Sun. The models do not include absorption from the interstellar medium and can therefore be directly applied to investigations of photochemistry and stability of exoplanet atmospheres.

The temperature profiles for the models consist of a linear structure in the chromosphere and transition region. We find that nearly the same set of parameters ( $\nabla T_{TR} = 10^9$  K dyne $^{-1}$  cm $^2$ ,  $m_{TR} = 10^{-6.5}$  g cm $^{-2}$ ,  $m_{Tmin} \simeq 10^{-3.5}$  g cm $^{-2}$ ) best reproduces the UV observations for all three stars, suggesting that early M type stars may have similar thermal structures in their upper atmospheres. These similarities, however, could also be a result of the simplified thermal structure averaging out small differences between the stars. Cool stars are highly active in their upper atmospheric layer with locally active regions of enhanced or depressed EUV flux. For example, spatially varying solar atmospheric features, for which there are high resolution spectra available, are modeled with several different thermal structures (Fontenla et al. 2011). Our simplified models provide general approximations of the EUV spectrum.

We find that our simplified structure produces similar continuum and line fluxes (for wavelengths greater than 200 Å) to the GJ 832 spectrum computed with the SSRPM semiempirical stellar atmosphere code, which includes a corona (Fontenla et al. 2016). The thermal structures in each model are significantly different

in the upper-most atmospheric layers, with the onset of the transition region beginning at a pressure nearly  $100\times$  lower and a temperature 3,000 K hotter in the PHOENIX model. To improve our general understanding of the upper atmospheric temperature-pressure profile and prediction of EUV fluxes, we will extend our thermal structures to coronal temperatures and quantify the importance of ambipolar diffusion in future work.

Starting in the early 2020s after *HST* stops UV operations, there will be an observation gap for FUV and NUV spectroscopy, in addition to the current gap in EUV observations for any star other than the Sun. During this time, there will be no instrument available to follow up with UV observations of newly discovered planet host stars. The expansive database of archival *GALEX* UV photometry for hundreds of M stars ranging in age and spectral type can be used to guide upper-atmosphere models such as these. These models predict realistic high resolution spectra across unobservable wavelengths and are important for furthering our understanding of the effects of high energy radiation on planets orbiting M stars.

This work was supported by NASA Headquarters under the NASA Earth and Space Science Fellowship Program-Grant NNX15AQ94H. E.S. acknowledges support from the NASA Habitable Worlds grant NNX16AB62G. We also gratefully acknowledge support from NASA HST Grant HST-GO-14784.001-A. An allocation of computer time from the UA Research Computing High Performance Computing (HPC) at the University of Arizona is gratefully acknowledged. A portion of the calculations presented here were performed at the Hochleistungs Rechenzentrum Nord (HLRN), and at the National Energy Research Su-



percomputer Center (NERSC), which is supported by the Office of Science of the U.S. Department of Energy under Contract No. DE-AC03-76SF00098. We thank all these institutions for a generous allocation of computer time. E.B. acknowledges support from NASA Grant NNX17AG24G. This work has made use of data from the European Space Agency (ESA) mission *Gaia* (<https://www.cosmos.esa.int/gaia>), processed

by the *Gaia* Data Processing and Analysis Consortium (DPAC, <https://www.cosmos.esa.int/web/gaia/dpac/consortium>). Funding for the DPAC has been provided by national institutions, in particular the institutions participating in the *Gaia* Multilateral Agreement.

*Software:* PHOENIX (Hauschildt 1993; Hauschildt & Baron 2006; Baron & Hauschildt 2007)

## REFERENCES

- Altmann, M., Roeser, S., Demleitner, M., Bastian, U., & Schilbach, E. 2017, *A&A*, 600, L4
- Ammons, S. M., Robinson, S. E., Strader, J., et al. 2006, *ApJ*, 638, 1004
- Andretta, V., & Giampapa, M. S. 1995, *ApJ*, 439, 405
- Andretta, V., Doyle, J. G., & Byrne, P. B. 1997, *A&A*, 322, 266
- Anglada-Escudé, G., Amado, P. J., Barnes, J., et al. 2016, *Nature*, 536, 437
- Ayres, T. R. 1979, *ApJ*, 228, 509
- Bailey, J., Butler, R. P., Tinney, C. G., et al. 2009, *ApJ*, 690, 743
- Baron, E., & Hauschildt, P. H. 2007, *A&A*, 468, 255
- Barstow, M. A., & Holberg, J. B. 2007, *Extreme Ultraviolet Astronomy*, by Martin A. Barstow, Jay B. Holberg, Cambridge, UK: Cambridge University Press, 2007
- Bianchi, L., Herald, J., Efremova, B., et al. 2011, *Ap&SS*, 335, 161.
- Bourges, L., Lafrasse, S., Mella, G., et al. 2014, *Astronomical Data Analysis Software and Systems XXIII*, 485, 223
- Butler, R. P., Vogt, S. S., Marcy, G. W., et al. 2004, *ApJ*, 617, 580
- Butler, R. P., Howard, A. W., Vogt, S. S., & Wright, J. T. 2009, *ApJ*, 691, 1738
- Chadney, J. M., Galand, M., Unruh, Y. C., Koskinen, T. T., & Sanz-Forcada, J. 2015, *Icarus*, 250, 357
- Craig, N., Abbott, M., Finley, D., et al. 1997, *ApJS*, 113, 131
- Cutri, R. M., Skrutskie, M. F., van Dyk, S., et al. 2003, *VizieR Online Data Catalog*, 2246
- Del Zanna, G., Landini, M., & Mason, H. E. 2002, *A&A*, 385, 968
- Del Zanna, G., Storey, P. J., Badnell, N. R., et al. 2014, *A&A*, 565, A77.
- Del Zanna, G., Dere, K. P., Young, P. R., Landi, E., & Mason, H. E. 2015, *A&A*, 582, A56
- Dere, K. P., Landi, E., Mason, H. E., Monsignori Fossi, B. C., & Young, P. R. 1997, *A&AS*, 125, 149
- Dere, K. P., Del Zanna, G., Young, P. R., et al. 2019, *ApJS*, 241, 22
- Donnelly, R. F., White, O. R., & Livingston, W. C. 1994, *SoPh*, 152, 69
- Dressing, C. D., & Charbonneau, D. 2013, *ApJ*, 767, 95
- Dressing, C. D., & Charbonneau, D. 2015, *ApJ*, 807, 45
- Droege, T. F., Richmond, M. W., Sallman, M. P., & Creager, R. P. 2006, *PASP*, 118, 1666
- Ehrenreich, D., Bourrier, V., Wheatley, P. J., et al. 2015, *Nature*, 522, 459
- Eriksson, K., Linsky, J. L., & Simon, T. 1983, *ApJ*, 272, 665
- Fontenla, J., Reichmann, E. J., & Tandberg-Hanssen, E. 1988, *ApJ*, 329, 464
- Fontenla, J. M., Avrett, E. H., & Loeser, R. 1990, *ApJ*, 355, 700
- Fontenla, J. M., Balasubramaniam, K. S., & Harder, J. 2007, *ApJ*, 667, 1243
- Fontenla, J. M., Curdt, W., Haberleiter, M., Harder, J., & Tian, H. 2009, *ApJ*, 707, 482
- Fontenla, J. M., Harder, J., Livingston, W., Snow, M., & Woods, T. 2011, *Journal of Geophysical Research (Atmospheres)*, 116, D20108
- Fontenla, J. M. 2013, *AGU Fall Meeting Abstracts 2013*, A23B-0223
- Fontenla, J. M., Landi, E., Snow, M., & Woods, T. 2014, *Solar Physics*, 289, 515
- Fontenla, J. M., Stancil, P. C., & Landi, E. 2015, *ApJ*, 809, 157
- Fontenla, J. M., Linsky, J. L., Witbrod, J., et al. 2016, *ApJ*, 830, 154
- Forveille, T., Bonfils, X., Delfosse, X., et al. 2009, *A&A*, 493, 645
- Fossati, L., Haswell, C. A., Froning, C. S., et al. 2010, *ApJL*, 714, L222
- Fossati, L., Marcelja, S. E., Staab, D., et al. 2017, *A&A*, 601, A104
- France, K., Froning, C. S., Linsky, J. L., et al. 2013, *ApJ*, 763, 149
- France, K., Parke Loyd, R. O., Youngblood, A., et al. 2016, *ApJ*, 820, 89

- France, K., Arulanantham, N., Fossati, L., et al. 2018, *ApJS*, 239, 16
- Fuhrmeister, B., Schmitt, J. H. M. M., & Hauschildt, P. H. 2005, *A&A*, 439, 1137
- Fuhrmeister, B., Short, C. I., & Hauschildt, P. H. 2006, *A&A*, 452, 1083
- Gaia Collaboration, Brown, A. G. A., Vallenari, A., et al. 2018, *A&A*, 616, A1
- Gaidos, E., Mann, A. W., Lépine, S., et al. 2014, *MNRAS*, 443, 2561
- Giampapa, M. S., Worden, S. P., & Linsky, J. L. 1982, *ApJ*, 258, 740
- Gillon, M., Triaud, A. H. M. J., Demory, B.-O., et al. 2017, *Nature*, 542, 456
- Gizis, J. E., Reid, I. N., & Hawley, S. L. 2002, *AJ*, 123, 3356
- Gomes da Silva, J., Santos, N. C., Bonfils, X., et al. 2011, *A&A*, 534, A30
- Guinan, E. F., Engle, S. G., & Durbin, A. 2016, *ApJ*, 821, 81
- Hauschildt, P. H. 1993, *JQSRT*, 50, 301
- Hauschildt, P. H., Allard, F., Alexander, D. R., Schweitzer, A., & Baron, F. 1996, *Stellar Surface Structure*, 176, 539
- Hauschildt, P. H., & Baron, E. 2006, *A&A*, 451, 273
- Hawley, S. L., Allred, J. C., Johns-Krull, C. M., et al. 2003, *ApJ*, 597, 535
- Hintz, D., Fuhrmeister, B., Czesla, S., et al. 2019, *A&A*, 623, A136
- Houdebine, E. R. 2010, *A&A*, 509, A65
- Hu, R., Seager, S., & Bains, W. 2012, *ApJ*, 761, 166
- Huber, D., Bryson, S. T., & et al. 2017, *VizieR Online Data Catalog*, 4034
- Jevremović, D., Doyle, J. G., & Short, C. I. 2000, *A&A*, 358, 575
- Kopparapu, R. K. 2013, *ApJl*, 767, L8
- Koskinen, T. T., Yelle, R. V., Lavvas, P., & Lewis, N. K. 2010, *ApJ*, 723, 116
- Kretzschmar, M., Dudok de Wit, T., Lilensten, J., et al. 2009, *Acta Geophysica*, 57, 42
- Kulow, J. R., France, K., Linsky, J., et al. 2014, *ApJ*, 786, 132
- Kurucz, R. L. 2014, *Determination of Atmospheric Parameters of B-, A-, F- and G-Type Stars. Series: GeoPlanet: Earth and Planetary Sciences*, ISBN: 978-3-319-06955-5. Springer International Publishing (Cham), Edited by Ewa Niemczura, Barry Smalley and Wojtek Pych, pp. 63-73, 63
- Kurucz, R. L. 2017, *Including All the Lines: Data Releases for Spectra and Opacities through 2017. Workshop on Astrophysical Opacities 2017*
- Lammer, H., Lichtenegger, H. I. M., Kulikov, Y. N., et al. 2007, *Astrobiology*, 7, 185
- Landi, E., Del Zanna, G., Young, P. R., et al. 2006, *ApJS*, 162, 261
- Lanotte, A. A., Gillon, M., Demory, B.-O., et al. 2014, *A&A*, 572, A73
- Lasker, B. M., Lattanzi, M. G., McLean, B. J., et al. 2008, *AJ*, 136, 735
- Lecavelier Des Etangs, A. 2007, *A&A*, 461, 1185
- Lemaire, P., Emerich, C., Curdt, W., Schuehle, U., & Wilhelm, K. 1998, *A&A*, 334, 1095
- Linsky, J. L., & Avrett, E. H. 1970, *PASP*, 82, 169
- Linsky, J. L., Fontenla, J., & France, K. 2014, *ApJ*, 780, 61
- Linsky, J. *Annual Review of Astronomy and Astrophysics*, 2017, 55, 159
- Louden, T., Wheatley, P. J., Irwin, P. G. J., Kirk, J., & Skillen, I. 2017, *MNRAS*, 470, 742
- Loyd, R. O. P., France, K., Youngblood, A., et al. 2016, *ApJ*, 824, 102
- Parke Loyd, R. O., Shkolnik, E. L., Schneider, A. C., et al. 2018, *ApJ*, 867, 70
- Loyd, R. O. P., France, K., Youngblood, A., et al. 2018, *ApJ*, 867, 71
- Luger, R., & Barnes, R. 2015, *Astrobiology*, 15, 119
- Monsignor Fossi, B. C., Landini, M., Del Zanna, G., & Bowyer, S. 1996, *ApJ*, 466, 427
- Moses, J. I. 2014, *Philosophical Transactions of the Royal Society of London Series A*, 372, 20130073
- Murray-Clay, R. A., Chiang, E. I., & Murray, N. 2009, *ApJ*, 693, 23
- Narain, U., & Ulmschneider, P. 1996, *SSRv*, 75, 453
- Neves, V., Bonfils, X., Santos, N. C., et al. 2013, *A&A*, 551, A36
- Neves, V., Bonfils, X., Santos, N. C., et al. 2014, *A&A*, 568, A121
- Newton, E. R., Irwin, J., Charbonneau, D., et al. 2016, *ApJ*, 821, 93
- Ofek, E. O. 2008, *PASP*, 120, 1128
- Peacock, S., Barman, T., Shkolnik, E. L., Hauschildt, P. H., & Baron, E. 2019, *ApJ*, 871, 235
- Rahmati, A., Cravens, T. E., Nagy, A. F., et al. 2014, *Geophysical Research Letters*, 41, 4812
- Rauscher, E., & Marcy, G. W. 2006, *Publications of the Astronomical Society of the Pacific*, 118, 617.
- Robinson, R. D., Linsky, J. L., Woodgate, B. E., et al. 2001, *ApJ*, 554, 368
- Röser, S., Schilbach, E., Schwan, H., et al. 2008, *A&A*, 488, 401
- Roeser, S., Demleitner, M., & Schilbach, E. 2010, *AJ*, 139, 2440

- Rugheimer, S., Kaltenegger, L., Segura, A., Linsky, J., & Mohanty, S. 2015, *ApJ*, 809, 57
- Santos, N. C., Sousa, S. G., Mortier, A., et al. 2013, *A&A*, 556, A150
- Sanz-Forcada, J., Micela, G., Ribas, I., et al. 2011, *A&A*, 532, A6
- Schneider, A. C., & Shkolnik, E. L. 2018, *AJ*, 155, 122
- Segura, A., Kasting, J. F., Meadows, V., et al. 2005, *Astrobiology*, 5, 706
- Segura, A., Walkowicz, L. M., Meadows, V., Kasting, J., & Hawley, S. 2010, *Astrobiology*, 10, 751
- Shields, A. L., Ballard, S., & Johnson, J. A. 2016, *PhR*, 663, 1
- Shkolnik, E. L., & Barman, T. S. 2014, *AJ*, 148, 64
- Short, C. I., & Doyle, J. G. 1998, *A&A*, 336, 613
- Sim, S. A., & Jordan, C. 2005, *MNRAS*, 361, 1102
- Soubiran, C., Le Campion, J.-F., Brouillet, N., & Chemin, L. 2016, *A&A*, 591, A118
- Staaath, E., & Lemaire, P. 1995, *A&A*, 295, 517
- Stelzer, B., Marino, A., Micela, G., et al. 2013, *MNRAS*, 431, 2063
- Suárez Mascareño, A., Rebolo, R., González Hernández, J. I., & Esposito, M. 2015, *MNRAS*, 452, 2745
- Terrien, R. C., Mahadevan, S., Deshpande, R., & Bender, C. F. 2015, *ApJS*, 220, 16
- Tian, F., Kasting, J. F., Liu, H.-L., & Roble, R. G. 2008, *Journal of Geophysical Research (Planets)*, 113, E05008
- Tian, H., Curdt, W., Marsch, E., & Schühle, U. 2009, *A&A*, 504, 239
- Tilley, M. A., Segura, A., Meadows, V., et al. 2019, *Astrobiology*, 19, 64
- Tobiska, W. K. 1996, *Advances in Space Research*, 18, 3
- Torres, G. 2007, *ApJ*, 671, L65
- Trainer, M. G., Pavlov, A. A., Dewitt, H. L., et al. 2006, *Proceedings of the National Academy of Science*, 103, 18035
- Triaud, A. H. M. J., Lanotte, A. A., Smalley, B., & Gillon, M. 2014, *MNRAS*, 444, 711
- Trifonov, T., Kürster, M., Zechmeister, M., et al. 2018, *A&A*, 609, A117
- Tripathi, A., Kratter, K. M., Murray-Clay, R. A., & Krumholz, M. R. 2015, *ApJ*, 808, 173
- Vernazza, J. E., Avrett, E. H., & Loeser, R. 1981, *ApJS*, 45, 635
- Vogt, S. 2011, Keck Observatory Archive HIRES, id.U027Hr, U027Hr
- von Braun, K., Boyajian, T. S., van Belle, G. T., et al. 2014, *MNRAS*, 438, 2413
- Ward-Duong, K., Patience, J., De Rosa, R. J., et al. 2015, *MNRAS*, 449, 2618
- West, A. A., Weisenburger, K. L., Irwin, J., et al. 2015, *ApJ*, 812, 3
- Wittenmyer, R. A., Tuomi, M., Butler, R. P., et al. 2014, *ApJ*, 791, 114
- Wood, B. E., Redfield, S., Linsky, J. L., Müller, H.-R., & Zank, G. P. 2005a, *ApJS*, 159, 118
- Wordsworth, R. D., Forget, F., Selsis, F., et al. 2010, *A&A*, 522, A22
- Youngblood, A., France, K., Parke Loyd, R. O., et al. 2016, *ApJ*, 824, 101
- Youngblood, A., France, K., Loyd, R. O. P., et al. 2017, *ApJ*, 843, 31
- Zacharias, N., Finch, C. T., Girard, T. M., et al. 2012, *VizieR Online Data Catalog*, 1322